Applied Catalysis A, General 709 (2026) 120616

Contents lists available at ScienceDirect

Applied Catalysis A, General

journal homepage: www.elsevier.com/locate/apcata

NH_3 decomposition activity of Ru supported on hydrothermally derived carbon: Temperature effectson the morphological evolution

Miranda Guci [a,d,*], Markus Knäbbeler-Buß [a], Emma Verkama [a], Michael Günthel [a], Md Redwanul Islam [b], Lorenz Kienle [b], Erisa Saraçi [c,d], Jan-Dierk Grunwaldt [c,d], Florian Nestler [a]

[a] Fraunhofer Institute for Solar Energy Systems ISE, Heidenhofstraße 2, Freiburg im Breisgau 79110, Germany
[b] Department of Material Science, Kiel University, Kaiserstraße 4, Kiel 24143, Germany
[c] Institute of Catalysis Research and Technology, Karlsruhe Institute of Technology (KIT), Hermann-von-Helmholtz-Platz 1, Eggenstein-Leopoldshafen 76344, Germany
[d] Institute for Chemical Technology and Polymer Chemistry, Karlsruhe Institute of Technology (KIT), Engesserstr. 20, Karlsruhe 76131, Germany

ARTICLE INFO

Keywords:
COx-free hydrogen generation
Ammonia decomposition
Ruthenium
Hydrothermal carbonization
Pyrolysis

ABSTRACT

A hydrothermally derived carbon support was synthesized from the sustainable feedstock chitosan, with optional subsequent pyrolysis at 600 °C and 1000 °C, to explore its potential as a catalyst support material for ruthenium (Ru). The catalysts were prepared through wet impregnation using Ru nitrosyl nitrate as the precursor. Their catalytic performances in ammonia decomposition were investigated under conditions of 5 % NH_3 at 1 bar, within a temperature range of 300 °C to 600 °C, and a weight hourly space velocity of 15.000 $ml_N\ g_{cat}^{-1}\ h^{-1}$. The analytical techniques employed in this study included elemental analysis, thermogravimetric analysis (TGA), gas adsorption measurements, Raman spectroscopy, X-ray diffraction (XRD), flame atomic absorption spectroscopy (F-AAS), scanning transmission electron microscopy (STEM), hydrogen-based temperature-programmed reduction (H_2-TPR) and X-ray photoelectron spectroscopy (XPS). They unraveled that non-pyrolyzed supports showed a strong tendency for Ru agglomeration, whereas pyrolyzed supports exhibited improved metal distribution, which correlated with enhanced catalytic activity exceeding 50 % ammonia conversion at 450 °C. The surface chemistry of the carbon support was modified by varying the pyrolysis temperature, which affected the concentrations and types of oxygen and nitrogen surface groups. These changes altered the interaction between Ru and these surface groups. During the decomposition of the Ru precursor and the reduction of Ru oxides, the partial breakdown of oxygen and nitrogen surface groups led to surface reconstructions of the Ru nanoparticles, thereby affecting their crystallinity. This phenomenon was also observed during the catalytic testing, which was more pronounced on the HC-600 support. Modifying the surface chemistry of hydrochar via pyrolysis affects Ru distribution, reducibility, and crystallinity, thereby enhancing the NH_3 decomposition performance.

1. Introduction

Hydrogen (H_2) can serve as a clean energy source across various sectors. The establishment of a hydrogen economy is considered crucial to reduce greenhouse gas emissions and to address climate change. However, in terms of energy storage, the most prominent drawback of H_2 is its low volumetric energy density of 2.71 kWh/m^3 at STP [1–4]. This issue can be addressed by pressurization, cryogenic liquefication and/or adsorption of H_2 as well as the chemical conversion with carbon oxides or nitrogen (N_2) to gases or liquids with beneficial storage and handling properties [5,6]. Currently, extensive research is ongoing in the field of chemical H_2 carriers to cover the H_2 needs of the energy and chemical sector by a global trade infrastructure [5]. Among discussed carrier technologies, chemical conversion of H_2 to methane (CH_4), methanol (CH_3OH), dimethyl ether (C_2H_6O), liquid organic H_2 carriers (LOHC) such as dibenzyl toluene or to ammonia (NH_3) are considered [7]. All those molecules are regarded as the most promising options for international H_2 transport due to their high H_2 storage densities and easier handling [8–11]. In comparison to other chemical storage compounds, NH_3 exhibits several outstanding storage properties:

1) A high volumetric hydrogen density of 108 kg H_2/m^3 (at 20 °C and 8.6 bar) and specific energy density of 5.18 kWh/kg of liquefied ammonia [12].

* Corresponding author at: Fraunhofer Institute for Solar Energy Systems ISE, Heidenhofstraße 2, Freiburg im Breisgau 79110, Germany.
E-mail address: miranda.guci@ise.fraunhofer.de (M. Guci).

https://doi.org/10.1016/j.apcata.2025.120616
Received 9 July 2025; Received in revised form 29 September 2025; Accepted 30 September 2025
Available online 1 October 2025

2) An established infrastructure for ammonia production, transportation, and storage due to its global significance in the fertilizer industry facilitating the integration of ammonia as a H_2 carrier [13].
3) In contrast to other chemical H_2 carriers, the absence of carbon in the molecule allows for its synthesis and decomposition independently of any carbon source or capture, respectively.

A key challenge in using ammonia as a H_2 carrier lies in an efficient H_2 recovery by catalytic splitting into N_2 and H_2 [14], described by the following reaction equation:

$$NH_3 \rightleftharpoons N_2 + 3\ H_2\ \Delta H = +\ 92.4\ kJ\ mol^{-1} \quad (1)$$

Thermodynamically, this endothermic volume-expanding equilibrium reaction is favored by high temperatures and low pressures. However, as the availability of high-temperature heat utilities will decrease by the fossil fuels phase-out, temperature for the decomposition should be kept as low as possible [15]. To efficiently conduct NH_3 decomposition at temperatures below 500 °C, highly active catalytic systems are crucial to decrease the activation energy barrier [16].

In scientific literature, two rate-determining steps depending on the reaction conditions are described [17]: the cleavage of the first N-H bond and N_2 desorption. According to Sabatier's principle, an ideal catalyst with an appropriate adsorption energy accelerates the cleavage reaction while effectively releasing the products [18]. At low temperatures, the N_2 desorption step is identified as the rate-determining step, irrespective of the catalyst used [4]. Consequently, the metal-N binding energy becomes a key parameter for catalyst design. Boisen et al. demonstrated through experimental data that the relationship between the ammonia conversion rate and the nitrogen binding energy for various metals (Ru, Fe, Co, Ni, Cu) exhibits a volcano shape, with Ru positioned at the optimum point [19]. Fe is positioned on the left side of the volcano plot, indicating a stronger metal-N binding energy, with the potential of forming FeN_x [20]. In contrast, Co, Ni and Cu are located on the right side, signifying a weaker metal-N interaction. Therefore, most publications dealing with NH_3 decomposition use Ru as the active component [17–19]. Anyhow, the position of Ru on the volcano plot depends on the surface structure, e.g. Ru(0001) versus Ru step sites. The most active Ru sites in this structure-sensitive reaction are reported to be the B-5 sites, which correspond to step sites on hexagonal close-packed surfaces. It consists of an arrangement of three Ru atoms in one layer and two further Ru atoms in the layer directly above this at a monoatomic step on an Ru(0001) terrace [21]. Additionally, the electronic environment surrounding Ru can also influence the reactivity by modulating the difference between the energy of the center of the d-band (E_d) and the Fermi level (E_f), thereby altering the adsorption energies between Ru and the adsorbates [22].

Besides the active metal, the choice of the support greatly impacts the activity and stability of the catalyst. The most widely used supports for NH_3 decomposition are carbon- and metal oxide-based materials [23–27]. Among carbon-based materials, carbon nanotubes (CNTs) are currently under intense scientific investigation due to their unique properties such as high internal surface area and structural adaptability. The latter includes tunable shape and size, mechanical flexibility, surface functionalization, and integration into composites to enhance performance across various applications [28]. Besides CNTs, also carbon nanofibers (CNFs), carbon xerogels and graphitic carbons have been considered as supports for this application [29–32]. Yin et al. pioneered the use of Ru supported on CNTs, reporting that Ru/CNT catalysts exhibited a superior activity in ammonia decomposition compared to other supports, including AC, MgO, ZrO_2 and Al_2O_3. Furthermore, it was shown that the Ru particle size is support-dependent, ranging from 2 nm to 5 nm for CNTs, K/CNTs and AC, and from 3 nm to 15 nm on the metal oxides. These results suggested that using a support with both strong basicity and good electron conductivity could lead to a more efficient catalyst [33–35]. CNFs on the other hand are more cost-effective than CNTs and, as reported by Duan et al., demonstrate greater activity compared to Ru/CNTs. This enhanced performance is attributed to the improved electronic properties present at the edges of the CNFs [36,37]. Mazzone et al. introduced carbon xerogels derived from resorcinol-formaldehyde as a support for Ru. They further explored how CO_2 activation treatment at high temperatures along with nitrogen doping, enhanced the crystallinity of Ru. This improvement was also attributed to the basicity and electron donor effect [30].

In general, there has been an increased focus on heteroatom doping, such as oxygen and nitrogen as these modifications were shown to enhance the catalytic activity in NH_3 decomposition [38–41]. Garcia-Garcia et al. stated that oxygen surface groups, present on the surface of activated carbon, had a decisive effect on the achieved dispersion of active phase, influencing the electronic properties of the surface sites and stabilizing the materials against sintering phenomena [42]. Marco et al. investigated the effects of nitrogen doping on the activity of carbon-nanofiber-supported Ru nanoparticles in ammonia decomposition. Characterization techniques revealed that N-doping improved the electronic properties of the catalyst [43]. Support-mediated metal reduction maintained a higher ratio of metallic Ru in comparison to undoped or O-doped CNFs and reduced Ru sintering during the reaction. Another observed phenomenon was the increased electron donation from the support to the metal on N-doped CNFs compared to undoped and O-doped carbon, as confirmed by XPS. Moreover, the Ru metal uptake was 25 % higher on N-CNFs than on un-doped and O-doped CNFs, suggesting that pyridinic groups enhance metal precursor adsorption. However, unlike previous studies [44], no significant effect of nitrogen groups on Ru particle size after metal deposition was found.

Despite their potentials as catalyst carriers for NH_3 decomposition, some carbon materials exhibit certain individual disadvantages and limitations. CNTs and CNFs can be costly to produce and may reveal challenges related to their structural integrity and agglomeration [37]. While having a high surface area, carbon xerogels often suffer from poor electronic conductivity and mechanical stability [45].

To address the above-mentioned limitations of support materials for Ru-based catalysts, hydrothermal carbonization (HTC) emerges as a promising method, offering an environmentally friendly and resource-efficient approach for preparing carbonaceous materials. Moreover, the HTC process is scalable and straightforward, making it a favorable option for producing effective catalyst supports. Currently, HTC materials are scarcely discussed as catalyst carriers in gaseous reactions due to their typically low surface area [46]. To overcome this limitation, a subsequent pyrolysis can significantly enhance the material's porosity and surface area, while facilitating the incorporation of nitrogen functionalities into the carbon matrix [47]. The solid product known as hydrochar (HC) can be derived from sustainable precursor materials, such as biomass, organic waste, and biopolymers [48].

Among biopolymers, chitosan has gained significant attention in recent years due to its versatile properties, wide range of applications, and high availability [49–53]. Chemically, chitosan is a linear polysaccharide composed of β-(1→4)-linked D- glucosamine and N-acetyl-D-glucosamine units, giving it a partially deacetylated and nitrogen-containing structure [49]. It is derived from chitin, a naturally occurring biopolymer, which is found predominantly in the exoskeletons of crustaceans, insects, fungi, and cephalopods like squids [54] (see Fig. 1). The global annual production of chitin is estimated to approximately 6 Mt [55]. Commercially available chitosan contains impurities in the form of inorganic matter, which can further agglomerate during the carbon synthesis process. While some elements act as promoters, others do act as catalyst poisoning for the active sites in ammonia decomposition. To adjust the inorganic matter of organic materials, a combination of HTC with pyrolysis can be beneficial [56]. Reza et al. confirmed the effectiveness of HTC in removing inorganic matter from biomass through leaching, leading to a significant reduction in heavy metals of the resulting biochar. In their study, HTC treatment

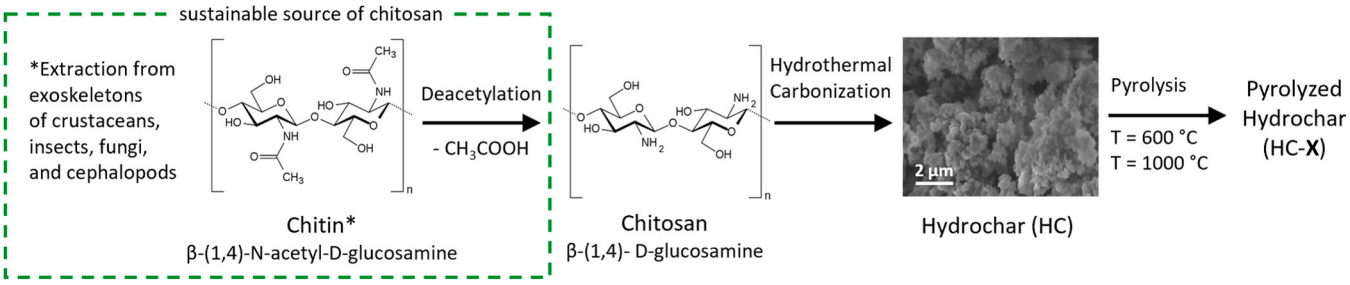

Fig. 1. Schematic illustration of the preparation procedure of hydrochar and pyrolyzed hydrochar from chitosan, including the sustainable source of chitosan. The SEM image of hydrochar is given.

also decreased slagging and fouling tendencies by lowering the alkali index and chlorine content, resulting in a cleaner and more efficient carbon material [57]. Therefore, following the HTC pathway has the potential to improve product quality by minimizing impurities.

To our knowledge, chitosan-derived hydrochar and pyrolyzed hydrochar have not yet been explored as potential supports for Ru. Furthermore, their role as supports for Ru or other metals in ammonia decomposition has not been investigated. Therefore, we aim to present this group of sustainable carbon materials as viable supports for Ru. Additionally, we want to examine the applicability of these catalysts in ammonia decomposition. Introducing heteroatoms such as oxygen or nitrogen to the carbon support can alter the surface chemistry to improve its adsorption capability towards the active metal. Our findings demonstrate that by tailoring those surface functionalities of hydrochar through pyrolysis, we can control the distribution, reducibility and crystallinity of Ru, which ultimately influences the catalytic activity in NH_3 decomposition.

2. Materials and methods

2.1. Carbon support and catalyst preparation

For the hydrochar (HC) preparation, chitosan (low molecular weight, Sigma Aldrich) was used as a precursor. Glacial acetic acid (99.9 %, Sigma Aldrich) was diluted to 20 vol.-% with deionized water. The HTC was carried out by mixing 28 g of chitosan with 350 ml of the 20 vol.-% acetic acid solution and thermally treating the mixture at 180 °C for 16 h in a 500 ml Carl-Roth autoclave. During HTC, the autogenous pressure in the system increased to 10 bar, which can be attributed to heating of process water leading to thermal expansion and water evaporation. The obtained solid material was washed out via Soxhlet extraction for at least 16 h using pure ethanol (99.98 %), and subsequent vacuum drying at 40 mbar for 6 h at 80 °C. Afterwards, two samples of the HTC solid product were pyrolyzed for 4 h in a quartz tube furnace under a continuous nitrogen (N_2) flow, resulting in the pyrolyzed hydrochar (HC-X). The carbon synthesis procedure is illustrated in Fig. 1. The pyrolysis temperatures were set to 600 °C and 1000 °C, respectively. Activated carbon NORIT® SX PLUS CAT, from here on labelled "AC", was used as a reference carbon material without any pretreatment.

Ru(III) nitrosyl nitrate (≥31.3 % Ru, ThermoFisher) served as the metal precursor for the catalyst synthesis. Wet impregnation (WI) was employed for the deposition of 1 wt.-% Ru metal onto the support materials, using ethanol (99.8 %) as a solvent. Finally, the catalysts were dried under vacuum conditions (50 mbar, 70 °C) and calcined at 400 °C for 2 h using an argon (Ar) atmosphere.

The supports were labelled as "HC" for synthesized hydrochar with the respective pyrolysis temperature of 600 °C and 1000 °C to obtain the following material descriptors: HC/HC-600/HC-1000. Once wet impregnated, "Ru" was added to the names of the respective materials.

2.2. Carbon support and catalyst characterization

Elemental analysis was conducted to determine the carbon, hydrogen, and nitrogen content in the bulk phase of the supports, calcined catalysts, and spent catalysts. The analysis was performed using a vario MICRO cube from Elementar, which is equipped with a thermal conductivity detector (TCD). The samples were crushed into a fine powder for ensuring representative results.

Thermogravimetric analysis (TGA) was conducted using a TGA 5500 from TA Instruments for chitosan and HC. Approximately 14 mg of sample were placed in a platinum crucible each of the measurements. The temperature program consisted of a heating rate of 10 K min^{-1} from room temperature to 815 °C, followed by an isothermal hold of 1 h. Using a flow rate of 20 ml_N min^{-1} the measurements were performed in air as well as in N_2 atmosphere. The measurements in air were repeated three times for each sample, with the average value reported as the ash content in chapter 3.1

N_2 adsorption and desorption isotherms of the supports and catalysts were collected using the surface area and pore size analyzer Nova800 from Anton Paar. The measurements were carried out at −196 °C, using liquid N_2 as the cooling agent. Prior to the measurements, 100 mg to 150 mg samples of the support or calcined catalyst were degassed at 200 °C for 3 h to remove moisture and other adsorbed species. The specific surface area (S_{BET}) was calculated using the Brunauer-Emmett-Teller (BET) equation [58] from the adsorption isotherms in the relative pressure range of 0.05–0.30. The quenched solid density functional theory (QSDFT) [59] was used for the calculation of pore size distribution, mean pore width (w_P), and total pore volume (V_T, p/p_0=0.95). Three repetitions of the support measurements were conducted using new samples from the same batch. The mean values are provided in Table 1, the respective standard deviations are provided in Table S2. Due to the limited sample availability, repetitions were not performed for the catalysts.

Raman spectra were acquired for all supports and catalysts using a WITec alpha500 high-resolution confocal spectrometer, employing a 532 nm laser as the excitation source. Three different spots for each sample were measured, and the average spectra were collected. To assess changes in the carbon structure, the I_D/I_G ratio was calculated by integrating the intensities of the D and G bands (D band at 1351 cm^{-1}; G band at 1586 cm^{-1}). The D band, associated with defects and the disordered structure of carbon, arises from the breathing modes of sp^2 carbon rings, indicating the presence of structural imperfections typical of amorphous carbons [54]. In contrast, the G band, related to the graphitic or ordered arrangement of sp^2 sites, results from the in-plane vibrations of carbon atoms within the graphitic lattice [49,50].

The X-ray diffraction for the supports was performed in a Rigaku SmartLab diffractometer (9 kW, Cu-Kα, Hypix-3000). The measurements were taken with a Kβ filter on the receiving side.

The pH of the supports was measured using a pH probe from Mettler Toledo. A sample of 1 g of solid was dissolved in 50 ml of deionized water and stirred for 1 h prior to the measurement.

Flame atomic absorption spectroscopy (F-AAS) was the technique

Table 1
Material properties obtained for chitosan, supports and catalysts.

Sample	CHN analysis				Atomic ratios		F-AAS	Nitrogen gas adsorption			Raman	pH
	C (wt%)	H (wt%)	N (wt%)	O* (wt%)	H/C	N/C	Ru (wt%)	S_{BET} ($m^2\ g^{-1}$)	V_T ($cm^3\ g^{-1}$)	w_P (nm)	I_D/I_G (-)	-
Chitosan	40.2	7.2	7.0	45.6	2.03	0.15	n.a.	n.a.	n.a.	n.a.	n.a.	n.a
HC	57.7	5.2	6.2	30.7	1.09	0.09	n.a.	48	0.11	8.9	1.2	4.0
HC−600	81.1	2.6	7.5	8.6	0.39	0.08	n.a.	103	0.09	3.3	1.3	5.0
HC−1000	85.0	1.3	3.3	10.3	0.19	0.03	n.a.	102	0.10	3.8	1.7	5.2
AC	86.5	0.9	0.2	12.4	0.12	0.00	n.a.	1033	0.67	2.6	2.0	5.5
Ru/HC	67.1	3.5	8.0	20.5	0.63	0.10	1.1	161	0.21	5.2	1.1	n.a
Ru/HC−600	77.8	2.5	7.7	10.9	0.39	0.08	0.9	166	0.12	2.7	1.6	n.a
Ru/HC−1000	83.2	1.4	3.0	11.2	0.21	0.03	1.2	157	0.20	5.1	1.7	n.a
Ru/AC	87.4	1.0	0.4	10.2	0.14	0.00	1.0	994	0.63	2.5	n.a	n.a

* The O content was measured as follows: 100 – C (wt%) – H (wt%) – N (wt%). It includes the ash content.

applied to measure the Ru content of the catalysts. A maximum of 250 mg of each sample was weighed into a Teflon vessel, sequentially treated with 5 ml of 35 % HCl and 20 ml of 69 % HNO_3, then sealed and heated to 200 °C within 15 min in a microwave oven at a maximum power of 650 W. After 30 min of digestion, the sample was cooled to approximately 30 °C, with a blank sample processed similarly to check for contamination. The clear solution was decanted, diluted to 50 ml with double-distilled water, and further diluted with 0.1 mol-% $CsCl_2$ in a 1 % HCl solution for analysis. The Ru content was analyzed at a wavelength of 349.89 nm, with a calibration performed prior to the analysis. A duplicate determination was conducted, the mean values are given in Table 1, the standard deviations are given in Table S2.

The scanning electron microscopy (SEM) measurements of the HC were conducted using a thermal field emission scanning electron microscope (FE-SEM) with a Schottky emitter, equipped with a GEMINI® electron column. The images were acquired at an acceleration voltage of 5 kV, employing an InLens secondary electron detector.

The scanning transmission electron microscopy (STEM) measurements of the reduced Ru catalyst on carbon-based support materials were performed in a probe corrected JEOL NeoARM 200 F microscope (200 kV). High angle annular dark field (HAADF, 80–220 mrad) detectors were used to achieve Z-contrast as well as atomic resolution of Ru particles on support matrix. Note that, to improve the sample quality for achieving maximum resolution, each TEM sample grids were heated at 200 °C inside a heating oven at ambient atmosphere to reduce contaminates (water solvents). From the HAADF images, the size of the Ru particles was measure manually for 1000 particles using the "Measure Features" tool at DigitalMicrograph software (GatanInc).

The reduction behavior of all samples was studied using temperature-programmed reduction (TPR) in diluted H_2. Prior to the measurements, all samples were dried at 200 °C for 2 h under Ar atmosphere. The TPR experiments were performed on an AMI- 300 from Altamira Instruments. The masses $m/z = 14$, 15, 16, 17, 18, 28, and 44 were monitored by an OmniStar GSD 350 mass spectrometer from Pfeiffer Vacuum. The temperature range for TPR was set between 30 °C and 400 °C, with a heating rate of 10 K min^{-1} and a total flow rate of 50 $ml_N\ min^{-1}$ containing 10 % H_2 in Ar. During this step, a heating rate of 10 K min^{-1} and a cooling rate of 50 K min^{-1} was employed.

X-ray photoelectron spectroscopy (XPS) was performed to investigate the elemental composition and the chemical states of the elements in the surface of supports and catalysts. The photoelectron spectra were obtained using an EnviroESCA spectrometer from Specs GmbH (Phoibos-NAP) 150 analyzer, 1D Delay-Line Detector, monochromatic Al Kα radiation at 1486.6 eV, incident angle 55°). The samples were prepared as powders on a conductive carbon tape. A microscopic check confirmed a closed and dense layer. All spectra were measured at a temperature of 298 K and a pressure of 7 × 10–7 mbar utilizing a pass energy of 30 eV (40 accumulations for C 1s, O 1s, Ru 3d; 150 accumulations for Ru 3p, 80–100 accumulations for N 1s support and 100–200 for N 1s catalyst). The photoelectron spectra of HC and HC 600 have shown significant surface charging under conventional XPS conditions. Therefore, NAP-XPS was applied using water vapor at a gas pressure of 3 mbar for charge compensation. Consequently, the resulting O 1s photoelectron spectra of these two samples contain signals of adsorbed water and the applied water vapor in the gas phase (between 534.3 eV and 535.4 eV). These signals were considered during the data evaluation but not further investigated. The calibration of the energy scale was performed using the Au 4f7/2 (83.96 eV) and Ag 3d5/2 (368.21 eV) photoelectron peaks.

The XPS data was processed with CasaXPS by applying the following peak fitting settings: The evaluation of the Ru 3d and Ru 3p signals was done considering spin doublet separation (DS-Ru 3d = 4.17 eV and DS-Ru 3p = 22.1 eV). For all spectra a Shirley background subtraction was applied. The C 1s signals were fitted using a Lorentzian line shape LA (1.643), for the Ru(0) species an asymmetric Lorentzian line shape LA (1.7,1.9,50) was used; for all other spectra a Gaussian-Lorentzian line shape GL(30) was applied. The spectra were charge-corrected based on the reference position of the C–C/C–H bonding peak of carbon at 285.0 eV. For semi-quantitative investigations relative sensitivity factors from CasaXPS were used.

2.3. Catalytic activity measurements

The catalytic activity of the Ru catalysts was screened in a fixed-bed flow reactor (AMI-300, Altamira Instruments) connected to a Matrix MG01C FTIR from Bruker with gas cell and a OmniStar GSD 350 mass spectrometer from Pfeiffer Vacuum. All samples were dried in helium (He) at 200 °C for 2 h and activated with 10 % H_2 in He at 400 °C for 1 h. During the drying and activation step, a heating rate of 10 K min^{-1} and a cooling rate of 50 K min^{-1} were employed. NH_3 decomposition was then carried out in a 5 % NH_3 in He atmosphere in the temperature range between 300 °C and 600 °C with 50 °C steps and respective holding times of 2 h at a heating rate of 10 K min^{-1}. At 450 °C, the experiments were repeated with a holding time of 16 h. During the activity measurements, a weight hourly space velocity (WHSV) of 15 000 $ml_N\ h^{-1}\ g_{cat}^{-1}$ was applied.

The following equations were used to calculate the weight hourly space velocity (WHSV), NH_3 conversion (X_{NH3}), NH_3 reaction rate (r) and H_2 production rate:

$$\mathrm{WHSV}\ \left[ml_N\ g_{cat}^{-1}\ h^{-1}\right] = \frac{\dot{V}_{feed}}{m_{cat}} \quad (2)$$

$$X_{NH3}\ [\%] = \frac{\dot{n}_{NH_3,inlet} - \dot{n}_{NH_3,outlet}}{\dot{n}_{NH_3,inlet}} \cdot 100\% \quad (3)$$

$$NH_3\ \text{reaction rate}\ \left[\text{mmol}\ NH_3\ g_{cat}^{-1}\ h^{-1}\right] = \frac{\dot{n}_{NH_3,inlet} - \dot{n}_{NH_3,outlet}}{m_{cat}} \quad (4)$$

$$H_2\ \text{production rate}\ \left[\text{mmol}\ H_2\ g_{cat}^{-1}\ h^{-1}\right] = 1.5 \cdot \frac{\dot{n}_{NH_3,inlet} - \dot{n}_{NH_3,outlet}}{m_{cat}} \quad (5)$$

$$\ln(r) = \ln(A) - \frac{E_a}{R} \cdot \frac{1000}{T} \quad (6)$$

Additional details on the calculation of the activation energy (E_a) are given in chapter 3.3 of the ESI. To enable a comparison of the experimental results to chemical equilibrium of NH_3 decomposition, minimization of Gibbs free energy was applied using the thermodynamic parameters for the relevant components with a temperature range between 300 °C and 600 °C, and at an absolute pressure of 1 bar [60]. Initial molar fractions were set in accordance with the experiments, i.e., 5 % NH_3 in inert atmosphere.

3. Results and discussion

The material properties of chitosan, the supports and catalysts are summarized in Table 1, including the chemical composition in bulk, Ru content in bulk, gas adsorption characteristics, structural properties from Raman analysis, and pH.

3.1. Support characterization

The chitosan used in this study contained 7.2 wt% nitrogen, enabling heteroatom doping of the carbon support, thus eliminating the need for an external nitrogen source (Table S1). In Fig. 1, a schematic illustration of the preparation procedure of the carbon support, including the sustainable source of chitosan, is given.

Chitosan underwent various decomposition reactions, including hydrolysis, dehydration, decarboxylation, polymerization, and aromatization, which is reflected in differences in the elemental composition of the non-pyrolyzed and pyrolyzed materials [61]. In particular, CHN analysis revealed that these reactions resulted in an absolute increase in carbon content of 17.5 wt% in the HC material, while the hydrogen (-2 wt%), oxygen (-14.9 wt%) and nitrogen content (-0.8 wt%) were reduced. During the dehydration step, water was released into the liquid phase, while the decarboxylation step resulted in the degradation of carboxyl and carbonyl groups. Simultaneously, the polymerization and aromatization reactions allowed carbon atoms to aggregate and form stable carbonaceous structures, thus increasing the overall carbon content in the bulk material [48,61]. Simsir et al. reported similar findings regarding chitosan, further indicating that extending the residence time during HTC from 18 h to 48 h resulted in only a 4.6 wt% increase in carbon content [62]. During pyrolysis of HC at 600 °C, further thermal decomposition occurred, leading to the breakdown of complex organic structures and the release of volatile compounds, which typically contain hydrogen and oxygen, as can be deduced from the CHN data in Table 1. This led to a further absolute increase in carbon and nitrogen content by 23.4 wt% and 1.3 wt%, respectively. Hydrogen and oxygen were lost as volatiles, reducing their overall concentrations. These results indicate that the hydrothermal carbonization of chitosan resulted in the formation of a nitrogen-rich carbonaceous material. During pyrolysis at 1000 °C, the thermal degradation of the HC intensified leading to a further decrease of hydrogen, oxygen as well as nitrogen to 1.3 wt%, 10.3 wt% and 3.3 wt%, respectively. Thus, the elevated temperature promoted the breakdown of nitrogen-containing functional groups, while the carbon content (85.0 wt%) further increased as the remaining char became more condensed and stable. Comparable findings were reported by Ramiro de Castro et al., who also investigated the nitrogen enrichment of chitosan-derived hydrochar at temperatures up to 800 °C (6.1 wt% nitrogen, 800°C). The chemical composition of the reference material AC resembles that of HC-1000, differing primarily in the absence of nitrogen.

In order to compare the thermal stability and oxidative decomposition of the HC materials with its feedstock chitosan, both N_2- and air-TGA measurements were conducted (Figure S1). N_2-TGA revealed a higher total mass loss for chitosan (77 wt%) up to 1000 °C, compared to HC (52 wt%). The initial thermal event between 50 °C and 200 °C for HC could be associated with moisture loss (e.g., physisorbed water), highlighting the increased water content due to the hydrothermal treatment compared to chitosan. The subsequent event, occurring from 200 °C onward, could be interpreted as the decomposition of volatile products, which is in alignment with the changes in the chemical composition (Table 1) [47]. Notably, for chitosan, the primary mass loss of approximately 40 wt% occurred around 300 °C, reflecting the breakdown of the polymer backbone into smaller volatile compounds [63]. This decomposition was less pronounced for HC since it had already undergone significant transformation during the HTC step. From 500 °C to 1000 °C, the thermal degradation pattern of both materials was in alignment, as further carbon structural transformations occurred alongside the release of residual volatiles.

In the air-TGA analysis, both samples exhibited complete combustion of organic compounds at 580 °C, with the residual mass corresponding to the ash content of 1.15 wt% for chitosan and 0.51 wt% for HC. While the measured ash content of chitosan is in alignment with the value given on the analysis certificate (Table S1), the reduced ash content after HTC suggested that some inorganic compounds were leached into the liquid phase during HTC [64]. However, it is to be noted that the TGA ash content has a certain degree of uncertainty due to the small amount of sample analyzed.

The temperature effect on the textural properties of the supports was studied by N_2 gas adsorption measurements. The adsorption and desorption isotherms as well as the pore size distributions can be found in Figure S2. According to the IUPAC classification, all isotherms show a type IV behavior, with a less pronounced hysteresis loop indicating pore condensation in the mesopores [65]. The increased N_2 adsorption uptake for $p/p_0 > 0.3$ is characteristic for porous carbons [66]. The specific surface area increased from HC to HC-600 from 48 $m^2\,g^{-1}$ to 103 $m^2\,g^{-1}$ and remained stable from HC-600 to HC-1000. In the isotherm profiles, the sharp rise at low relative pressures can be assigned to the presence of micropores, which is more pronounced in the thermally treated carbons. This presence of micropores may contribute to the increased specific surface area, likely resulting from the thermal decomposition of volatiles and the restructuring of the carbon scaffold. The pore width decreased with increased pyrolysis temperature from 8.9 nm to 3.3 nm and 3.8 nm for HC, HC-600, and HC-1000, respectively. The total pore volume remained stable throughout the support materials, being low with 0.1 $cm^3\,g^{-1}$ on average. In comparison to the HC materials, the reference material AC showed a higher specific surface area of 1033 $m^2\,g^{-1}$, total pore volume of 0.67 $cm^3\,g^{-1}$ and a smaller pore width of 2.6 nm.

To assess the overall carbonization degree of the materials, the H/C and N/C atomic ratios were calculated providing insights into the aromatic and aliphatic character of the bulk material. The H/C ratio of chitosan to HC-1000 decreased from 2.03 to 0.19, indicating an increase in aromaticity. The reference material AC exhibited the lowest H/C ratio of 0.12, linked to its aromatic structures formed by higher carbonization and removal of polar compounds, indicating the highest aromaticity [56]. Correspondingly, the N/C ratio decreased from 0.15 to 0.03, indicative of a more carbonized structure with diminished polar functional groups. The results by Zhao et al. support our findings, as their study revealed that chitosan-derived carbon materials exhibited a significant degree of aromaticity, as demonstrated by solid-state ^{13}C and ^{15}N NMR analyses. Moreover, their materials displayed improved electrical conductivity after subsequent calcination at 750 °C, with the nitrogen-doped samples demonstrating superior conductivity compared to the nitrogen-free counterparts [57]. Further structural changes can also be observed using Raman spectroscopy, as shown in Fig. 2. Both, the D and G band show an increased intensity with increased pyrolysis temperature, suggesting a higher graphitization degree. The D band appeared to be higher in intensity, which can be correlated with the formation of more structural imperfections due to the evolution of volatile components (see CHN analysis) and the breakdown of ordered graphitic domains [67]. The reference support AC shows a comparable trend as HC-1000, which also aligns with the low H/C ratios. The I_D/I_G

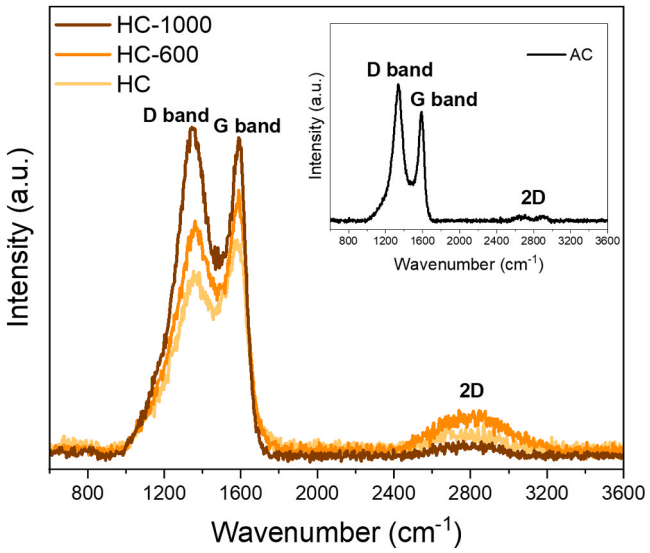

Fig. 2. Raman spectra of the HC-derived supports and the activated carbon (AC) as a reference.

ratios calculated from the integrated Raman peak areas show an increasing trend in the order: HC < HC-600 < HC-1000 < AC, indicating a greater increase in defects relative to the graphitic structure as the temperature rises.

The Raman results were also aligned with the XRD measurements shown in Figure S4, which provides additional insights into the structural characteristics of the carbon supports. The top panel of the figure displays the XRD pattern of graphite, characterized by sharp and distinct peaks corresponding to specific crystal planes, particularly the (002) plane at approximately $2\theta = 26.6°$ [68]. This serves as a reference for assessing the degree of graphitization in the samples below. In the bottom panel, XRD measurements from the HC-derived supports illustrate the evolution of graphitization. The reflection intensity in the region around the graphite (002) plane indicates how each sample compares to the well-ordered structure of graphite. HC-1000 shows the highest degree of graphitization, as evidenced by its narrower peaks ($FWHM_{HC\text{-}1000} < FWHM_{HC\text{-}600}$). Despite this trend, the calculated d-spacing for HC-1000 (approximately 3.53 Å) remains higher than that of standard turbostratic carbon (approximately 3.44 Å) [69], suggesting that the overall nature of the supports is still predominantly amorphous. In contrast, the commercial activated carbon exhibits more crystalline ordering, with sharper reflection intensities at specific 2θ values, including approximately 26.6°, 26.94°, and 28.1°, indicating a more developed graphitic structure. HC-600 also shows traces of ordering through minor intensity reflections, although these are too weak to decisively attribute to significant effects of pyrolysis. Overall, the XRD patterns highlight the transitional state of hydrochar-derived supports between amorphous carbon and more crystalline forms, highlighting their potential as alternatives to activated carbon.

From the pH measurements, the impact of the pyrolysis temperature on the oxygen content was reflected in a decreasing acidity. By means of pH, the value of 4.0 for HC (Table 1) indicated the presence of acidic surface functionalities, such as carboxyl, lactone, and phenol groups, as reported in literature [70]. Ketone, quinone, alcohol, and ether functionalities may contribute to the acidity, additionally [70]. The presence of these predominantly oxygenated functionalities results in a more hydrophilic and acidic carbon material with an increased surface charge density. Thus, post-HTC thermal treatment tunes the carbon surface towards less oxygenated functionalities, leading to a slight increase in basicity. This finding aligns with the results from CHN analysis. The reference material (AC) had a pH of 5.5, comparable to HC-1000.

The presence of nitrogen as an additional heteroatom on the support was also confirmed by XPS. The high-resolution N 1s photoelectron spectra were fitted with five subpeaks, representing pyridinic (N-1: 298.3–398.4 eV), amine (N-2: 299.4–299.5 eV), pyrrolic (N-3: 400.7–400.8 eV), quaternary (N-4: 401.8 eV) and oxidized (NO_x: > 402 eV) nitrogen species (Fig. 3, Table S6) [71–75]. HC exhibited two distinct nitrogen functionalities: amine and pyrrolic N, with surface concentrations of 44 at% and 56 at%, respectively. An additional peak observed at 398.4 eV for HC-600 can be attributed to the presence of pyridinic nitrogen, resulting from nitrogen incorporation during the thermal treatment process. This is consistent with the findings from CHN analysis, where a nitrogen-enrichment was observed. For HC-1000, an additional peak at 401.7 eV arised, which can be assigned to quaternary N, indicating a more graphitized carbon structure, which aligns with the Raman and XRD findings. The amine N peak disappeared due to the thermal treatment. In addition to that, peaks at higher binding energies (> 402 eV) appeared, and can be assigned to oxidized nitrogen species, such as pyridinic N oxide. We can conclude that elevated temperatures facilitate the transformation of pyrrolic and amine N into pyridinic (and its oxidized form) and quaternary N, presumably through polymerisation and condensation reactions [76,77].

The oxygen and nitrogen content on the carbon surface, as well as the O-to-N ratios, are presented in Table S7. Both, oxygen and nitrogen surface groups were removed through pyrolysis. The O-to-N ratio is highest for HC with 7, decreasing to 4.1 for HC-600 and to 1.3 for HC-1000. This finding highlights that HC and HC-600 have a greater presence of oxygen surface groups compared to nitrogen, while the O-to-N ratio is closer to 1 for HC-1000. This indicates that during the pyrolysis step, primarily oxygen-containing functional groups are decomposed up to 600 °C. As the temperature rises further to 1000 °C, nitrogen species are also removed. The chemical composition in bulk showed a comparable trend, with nitrogen enrichment up to 600 °C and then removal up to 1000 °C (see Table 1).

3.2. Catalyst characterization

The analysis results of the herein produced catalysts as well as the reference catalyst Ru/AC are listed in Table 1.

Due to the calcination step at 400 °C during the catalyst preparation, the bulk chemical composition changed in comparison to the supports. This effect was most pronounced for Ru/HC, as the support of this catalyst was not pyrolyzed prior to calcination, resulting in an increase in carbon content of 10 wt% and an enrichment in nitrogen by 0.8 wt%. For Ru/HC-600, the carbon content decreased by 3.3 wt% and the oxygen content decreased by 2.3 wt%, while the hydrogen and nitrogen content remained stable. García-García et al. reported in their study, that the NO_x species of the precursor $Ru(NO)(NO_3)_3$ are capable to oxidize the carbon support around Ru, leading to an increased content of carboxylic groups [42]. Those groups could decompose further and be released as CO/CO_2, likely resulting in a decrease of carbon content in Ru/HC-600. For Ru/HC-1000, a smaller decrease in carbon content of 1.8 wt% and nitrogen of 0.3 wt% was observed, indicating the additional decomposition of nitrogen.

The Ru loading measured by F-AAS ranged between 0.9 and 1.2 wt %. Marco et al. compared undoped CNFs with nitrogen and oxygen doped and came to the conclusion that the N-doped CNFs have a 25 % higher Ru uptake in comparison to the other supports [43]. This finding suggests that the presence of heteroatoms on the carbon surface affects the adsorption capacity of the Ru precursor.

Fig. 4 shows the STEM micrographs of the Ru catalysts along with particle size distributions. A comparison between the non-pyrolyzed Ru/HC and the pyrolyzed samples demonstrates that pyrolysis significantly affects the distribution of Ru nanoparticles on the carbon support. In the non-pyrolyzed HC support (Fig. 4a)), Ru particles tend to agglomerate, resulting in Ru-free regions on the support. In contrast, the pyrolyzed supports exhibit a diminished tendency for Ru agglomeration, leading to a more uniform metal distribution. This observation suggests an

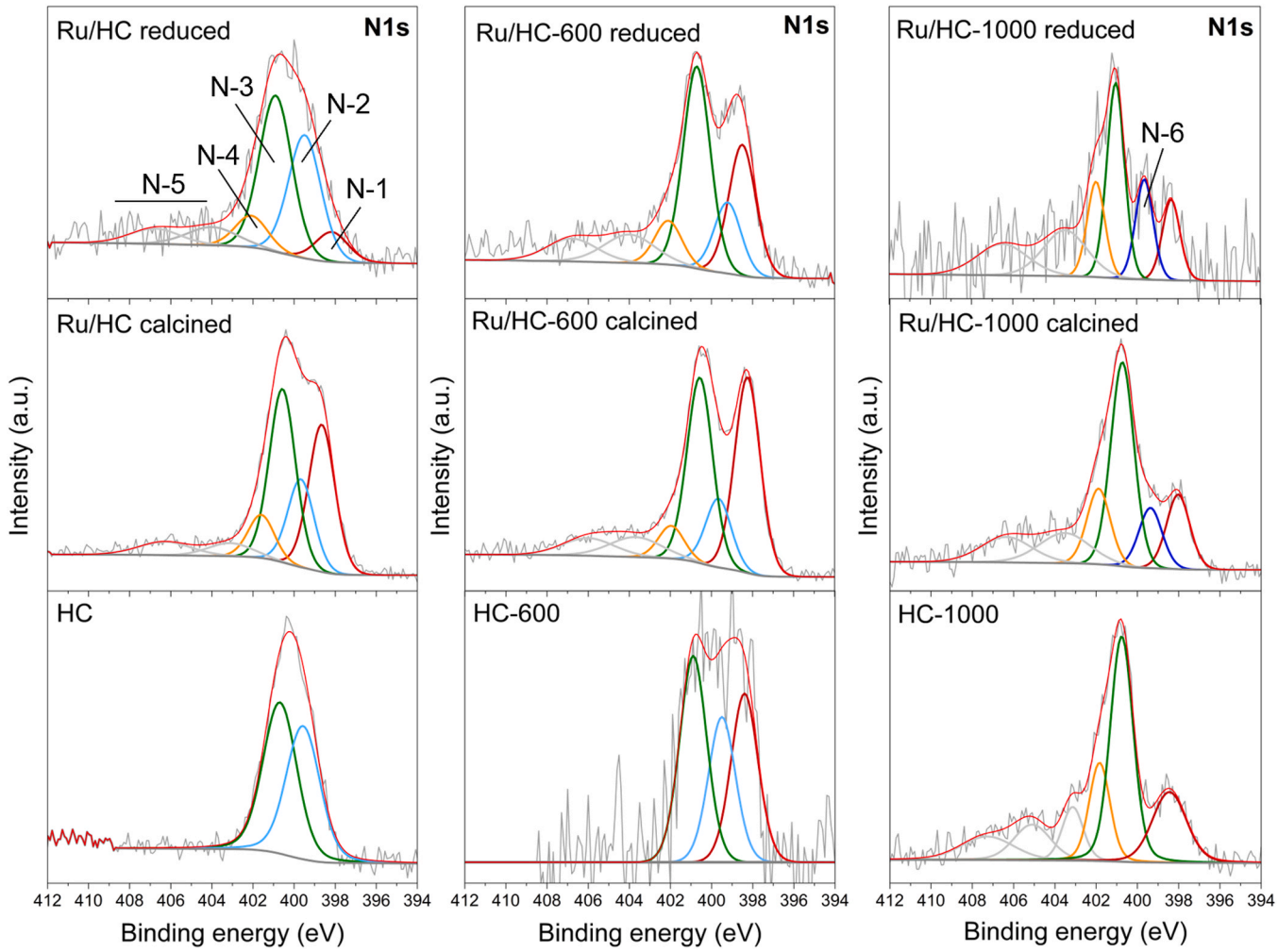

Fig. 3. High-resolution XPS spectra of N 1s for the supports, calcined and reduced catalysts with the following nitrogen species: N-1 Pyridinic-N, N-2 Amine-N, N-3 Pyrrolic-N, N-4 Quaternary-N, N-5 NO_x, N-6 Ru-N.

increased availability of anchoring sites on the pyrolyzed supports, as indicated by the XPS analysis presented in chapter 3.1. During carbon synthesis, we confirmed that thermal treatment effectively removed oxygen-containing groups, resulting in a decreased O-to-N ratio on the surface, which changed from 7 for HC to 1.3 for HC-1000 (Table S7). Conversely, nitrogen was successfully incorporated into the carbon matrix, with its content remaining stable from HC to HC-600, followed by a decrease in HC-1000. Additionally, the types of nitrogen species present on the HC-derived support changed following pyrolysis, with the appearance of pyridinic N and quaternary N. This transformation creates new anchoring sites for Ru, as supported by existing literature [43,78,79]. XRD confirmed an increased degree of graphitization upon pyrolysis, which, in addition to nitrogen functionalities, could contribute to the improved anchoring of Ru on the support (Figure S4) [80]. Compared to the pyrolyzed samples, Ru/AC exhibited a slightly denser particle distribution (Fig. 4d), likely due to its microporous structure [81]. High-resolution STEM micrographs of two individual type pristine Ru particles are demonstrated in Figure S6. The atomic resolution micrographs at the inset (i) of each figure indicate that the larger pristine particles are mostly hexagonal in shape. The average Ru size is small (1.3 nm to 1.5 nm) for all catalysts, including the Ru/AC reference, meaning that the Ru size is not impacted by support functionalization. Marco et al. reported similar findings, demonstrating that Ru was impregnated on both undoped and nitrogen- or oxygen-doped carbon nanofibers (CNFs) without affecting the average Ru particle size [43].

Fig. 5 displays the qualitative H_2-TPR profiles obtained for both, the supports and catalysts. The supports exhibited two low-intensity peaks at approximately 88 °C and above 300 °C, which can be attributed to the desorption of physisorbed water and to carbon support gasification, respectively. The formation of CO, CO_2, and CH_4 is expected in the presence of H_2 and at elevated temperatures, depending on the stability of the carbon support. Figure S3 presents the MS profiles for the masses 15 (CH_4), 28 (CO), and 44 (CO_2) during H_2-TPR analysis. For the HC sample, CO_2 formation begins at temperatures above 200 °C, as it has not been thermally treated at such high temperatures. In contrast, CO formation starts at temperatures above 300 °C, while CH_4 formation occurs at temperatures above 450 °C. The HC-600 sample is stable with respect to CH_4 formation up to 600 °C, but it begins to form CO_2 at temperatures above 250 °C, albeit with lower intensity compared to the HC sample. The HC-1000 sample also shows some CO_2 formation starting from 250 °C, but the quantity is comparatively small. In terms of CH_4 and CO formation, HC-1000 demonstrates significant stability. This stability is attributed to its higher degree of graphitization, as indicated by Raman spectroscopy (Fig. 2) and XRD measurements (Figure S4). The reference support AC remained stable as depicted in Fig. 5, which is also attributed to the higher graphitization degree, in alignment with HC-1000.

The HC-derived catalysts showed several peaks in the TPR spectra with different intensities. The first hydrogen consumption peak occurred between 88 °C and 133 °C, showing a shift towards higher temperatures from Ru/HC-1000 to Ru/HC. This shift suggests a stronger interaction between the Ru species and the support in the lower or non-pyrolyzed

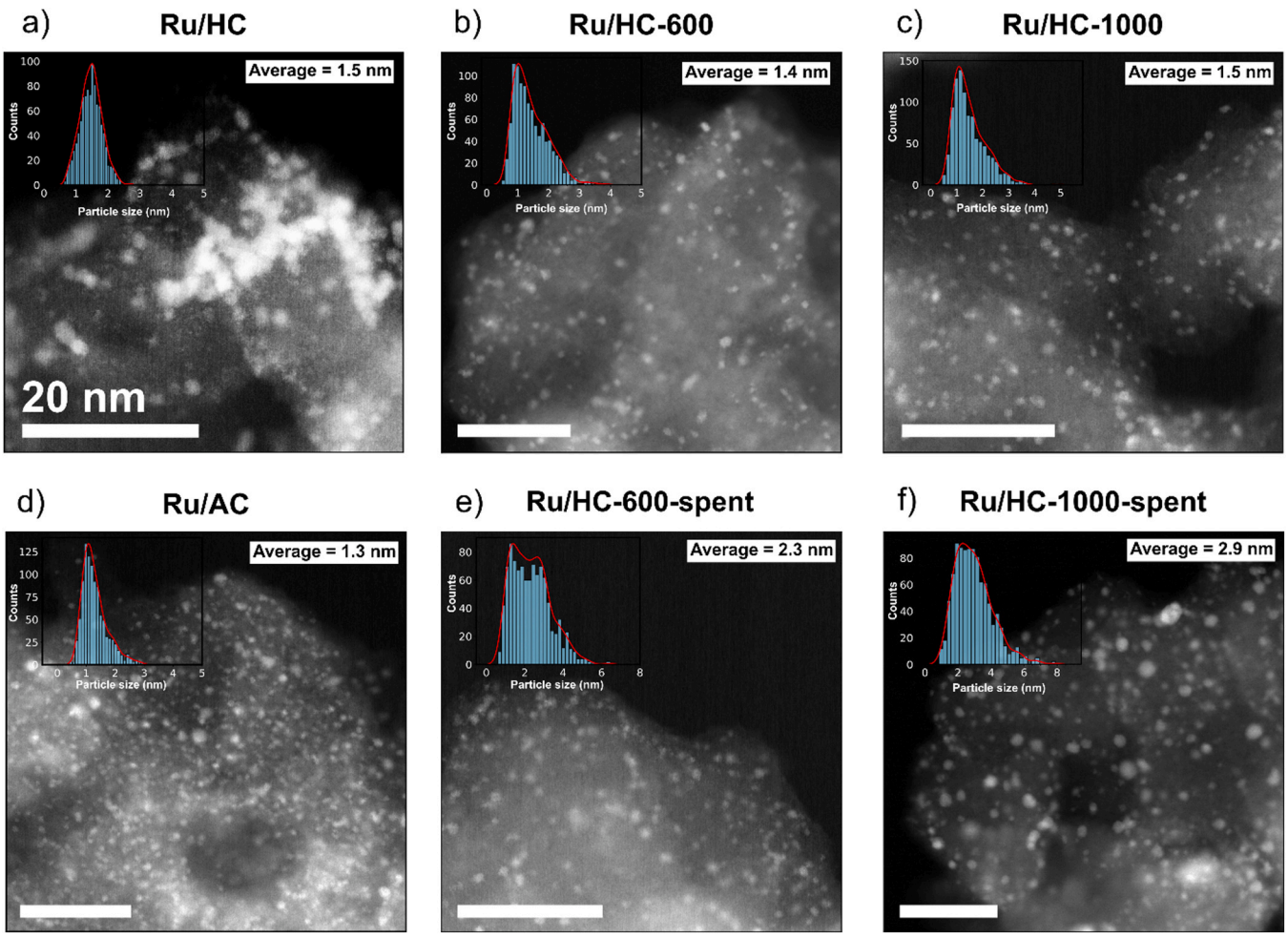

Fig. 4. STEM images of the ex-situ reduced catalysts a) Ru/HC, b) Ru/HC-600, c) Ru/HC-1000, d) Ru/AC and the corresponding histograms with the KDE line (solid, red) and spent catalysts (16 h, 450 °C) e) Ru/HC-600, and f) Ru/HC-1000 and the corresponding histograms with the KDE line (solid, red).

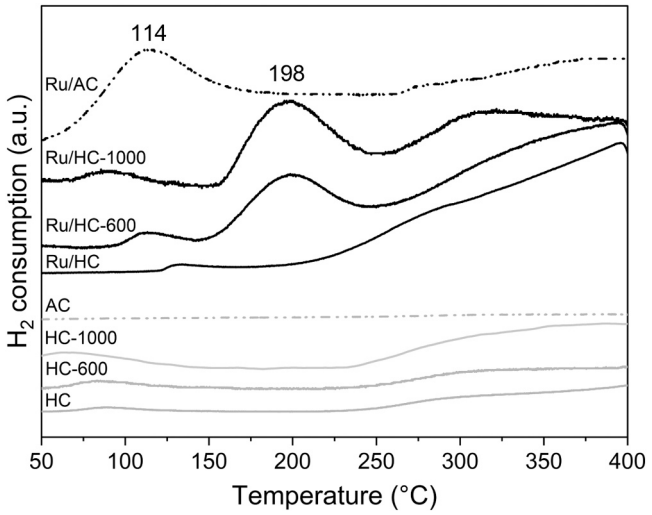

Fig. 5. Qualitative H_2-TPR profiles of the supports and Ru catalysts.

samples, potentially attributed to differences in surface chemistry. The O-to-N ratio is higher for HC and HC-600 (7.0 and 4.1) than for HC-1000 (1.3), indicating a greater availability of oxygen anchoring sites (Table S7). During calcination and reduction, the ratio decreased for Ru/HC and Ru/HC-600, while it increased for Ru/HC-1000. This indicates that nitrogen-containing groups were decomposed in the latter catalyst during these processes, highlighting the differences in metal-support interactions. In this context, Garcia-Garcia et al. have also investigated the role of oxygen surface groups in the reduction behavior of Ru when supported on activated carbon. Their findings indicate that the presence of oxygen groups facilitates a multi-step reduction process. During the reduction process, CO_2 is produced from the decomposition of carboxylic and lactone surface groups. This CO_2 can be adsorbed onto the surface of Ru nanoparticles, which helps stabilizing partially oxidized oxidation states of Ru. On the other hand, in the absence of oxygen-containing surface groups, a single-step Ru reduction has been observed [42].

A multi-step reduction process is also observed for the HC-derived catalysts, characterized by an additional consumption peak at 198 °C for both Ru/HC-600 and Ru/HC-1000. However, the second reduction peak is not present in the H_2-TPR spectra of Ru/HC. Additional hydrogen consumption peaks can be attributed to the gasification of the support surrounding the Ru particles, leading to CH_4 formation. This phenomenon is described in the literature as the H_2 spillover effect. Kowalcy et al. and Forni et al. reported that the methanation of carbon support can be decreased by increasing their degree of graphitization [82,83]. For our catalysts, however, we did not observe any differences in the amount of CH_4, which was measured qualitatively using a mass spectrometer (Figure S11). The reference catalyst Ru/AC displayed a main reduction peak at 114 °C, indicating a one-step reduction and a more compact Ru size distribution, as shown in Fig. 4d).

Fig. 3 presents the fitted N 1s spectra of the calcined and ex-situ

reduced catalysts with the following subpeaks: N-1 (pyridinic, 398.0–398.6 eV), N-2 (amine, 399.1–399.6 eV), N-3 (pyrrolic, 400.5–401.0 eV), N-4 (quaternary, 401.5–402.0 eV), N-5 (NO_x, >402 eV), N-6 (Ru-N, 399.3–399.6 eV) [39,71,72,84]. XPS analysis revealed that the nitrogen species on the surface changed after the Ru deposition on the non-pyrolyzed support. While the pyrrolic peak persisted, the amine peak diminished. Additionally, new peaks that correspond to pyridinic, quaternary, and oxygenated nitrogen species appeared (Table S6) [73]. This transformation is attributed to the calcination step at 400 °C, which increased the surface nitrogen concentration from 4.9 at% to 7.3 at%, as shown in Table S7. After the reduction of Ru/HC, the nitrogen content decreased from 7.3 at% to 1.6 at%. This reduction was facilitated by the presence of H_2, which catalyzed the decomposition of nitrogen groups. After metal deposition on HC-600, quaternary and oxygenated nitrogen species were formed, and the nitrogen content remained stable during the transition from the calcined to the reduced state (Table S7). In contrast, Ru/HC-1000 exhibited an additional peak (N-6, 399.6 eV) in both states, which can be assigned to pyridinic N coordinated to transition metals (M-N) [74]. This binding energy range has been previously reported for Ru-nitrogen interactions [85]. When the O-to-N surface ratio is close to 1, sufficient nitrogen sites are available, allowing Ru to coordinate with pyridinic N and giving rise to the Ru–N signal (Table S6, Table S7). In contrast, at an O-to-N ratio of 4 or higher the nitrogen density is too low, so Ru preferentially interacts with oxygenated groups instead. Due to that, no Ru–N species appeared in the N 1s spectra of Ru/HC and Ru/HC-600.

In literature, three different nitrogen species are discussed as potential anchoring sites for Ru: pyrrolic, pyridinic, and quaternary N. Both pyrrolic and pyridinic nitrogen atoms can donate p-electrons to the π-system, thereby enhancing the electronic properties of the carbon matrix. The resulting delocalization increases the local electron density, which strengthens the interaction with Ru and stabilizes the metal species [79,86]. In addition, pyridinic nitrogen provides a lone pair that can coordinate to the vacant orbital of Ru^{3+}, effectively anchoring the metal ion [87]. In contrast, graphitic nitrogen, which is embedded within the graphene plane, does not directly coordinate with Ru. However, it plays a crucial role in tuning the electronic environment, thereby enhancing the stability and conductivity of the carbon support [44,88].

When comparing the nitrogen species of the HC-derived supports, it is evident that pyridinic nitrogen may play a role in anchoring Ru nanoparticles. This species is absent in HC (Table S6), which resulted in a high tendency for Ru nanoparticles to clamp together, as confirmed by STEM analysis (Fig. 4). Pyridinic nitrogen is present in both HC-600 and HC-1000, while quaternary nitrogen is present only in HC-1000. Although the metal distribution is relatively good on both catalysts (Ru/HC-600 and Ru/HC-1000), we do not see a positive impact from quaternary nitrogen on metal distribution. Furthermore, pyrrolic nitrogen is present in all three supports, indicating that it also does not have a significant impact on the anchoring of Ru nanoparticles. Chen et al. have also reported pyridinic nitrogen as a potential anchoring site for Ru, which also impacted the average Ru particle size. In the case of our HC-derived catalysts, no impact of nitrogen species on the average Ru size has been observed (Table 1).

The component fit of the Ru $3p_{3/2}$ spectra into four symmetric components is shown in Fig. 6. The presence of oxidized Ru states, in addition to metallic Ru, is proven [84]. However, differentiating between the various Ru oxide species using only XPS is challenging due to potential overlap. García-García et al. reported that Ru^{3+} is oxidized by NO_x species during the impregnation, drying, and calcination of the Ru $(NO)(NO_3)_3$ precursor [42]. Consistent with this, we also observed the presence of Ru^{4+} in all catalysts. The additional oxide peaks observed around 462.6 eV, and 463.0 eV cannot be directly attributed to a specific species. In addition, the authors mentioned the presence of Ru^{3+} and Ru^{+} alongside Ru^{4+}, as determined from XANES measurements. In our study, a partial reduction of Ru oxides to metallic Ru during calcination occurred, most notably on HC, as indicated by the highest $Ru^0/Ru^{\delta+}$ ratio of 0.26 among all calcined samples (Table 2). As expected, the ex-situ reduced catalysts exhibit a more pronounced peak for metallic Ru, with the same $Ru^0/Ru^{\delta+}$ ratio of 0.42 for Ru/HC-600, Ru/HC-1000 and Ru/AC.

The binding energies of the different Ru species and their surface concentrations, determined from XPS-data analysis are listed in Table 2. The Ru surface concentration of the HC-derived calcined catalysts ranges from 0.8 at% to 0.9 at%. Ru/AC exhibits a lower surface concentration of 0.4 at%, which remains low even in its reduced state. Notably, the surface concentration for the reduced Ru/HC decreased from 0.8 at% to 0.2 at%. This can be attributed to the presence of less stable nitrogen groups, such as pyrrolic nitrogen, which may decompose in the presence of hydrogen, thereby removing Ru from the surface. For the other two catalysts, it increased up to 1.0 at% and 1.4 at%, respectively.

3.3. Activity measurements of Ru catalysts in ammonia decomposition

The activity measurements of the catalysts are illustrated in Fig. 7a).

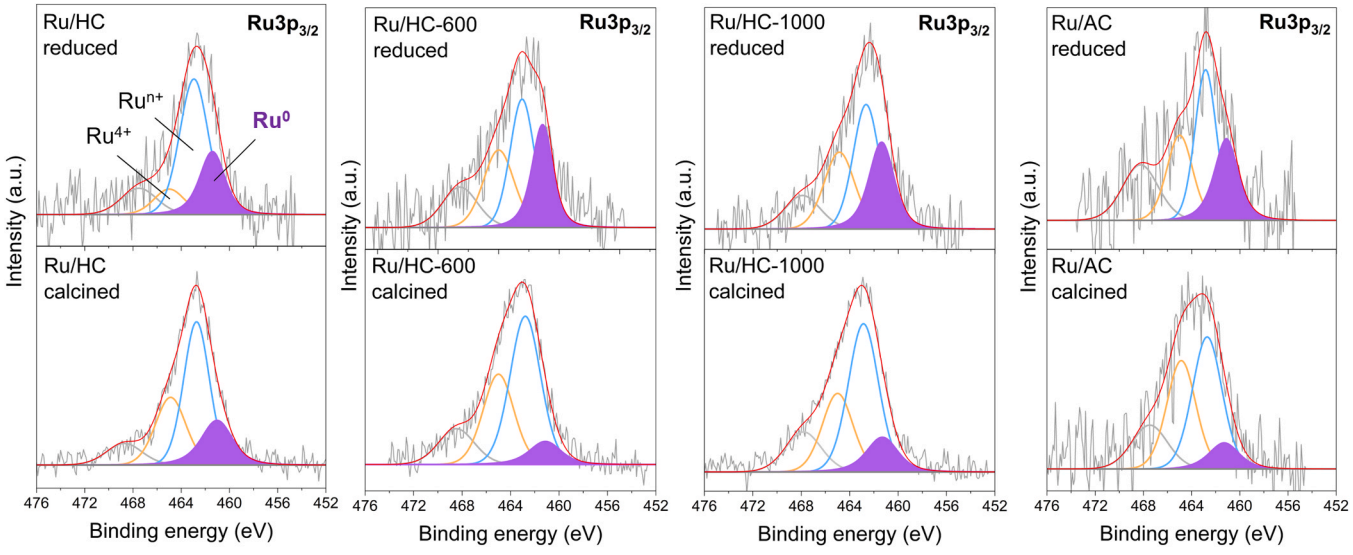

Fig. 6. High-resolution XPS spectra of Ru $3p_{3/2}$ for the supports, calcined and reduced catalysts with the Ru species: Ru^0, Ru^{n+}, Ru^{4+} and the satellite.

Table 2
Binding energies (B.E.) and at% of Ru3p$_{3/2}$ core level for calcined (calc.) and ex-situ reduced (red.) catalysts, including the nitrogen and oxygen content from XPS.

Catalysts	Ru^0		Ru^{n+}		Ru^{4+}		$Ru^0/Ru^{\delta+}$	Ru content
	B.E. (eV)	at%	B.E. (eV)	at%	B.E. (eV)	at%	-	at%
Ru/HC calc.	461.0	21	462.7	51	464.8	28	0.26	0.8
Ru/HC−600 calc.	461.1	10	462.7	56	465.0	34	0.11	0.8
Ru/HC−1000 calc.	461.2	15	462.8	55	465.0	30	0.17	0.9
Ru/AC calc.	461.1	12	462.7	49	464.8	39	0.13	0.4
Ru/HC red.	461.3	27	462.9	61	465.0	12	0.36	0.2
Ru/HC−600 red.	461.3	30	463.0	40	464.9	30	0.42	1.0
Ru/HC−1000 red.	461.3	30	462.6	41	464.7	29	0.42	1.4
Ru/AC red.	461.1	30	462.8	42	465.0	28	0.42	0.5

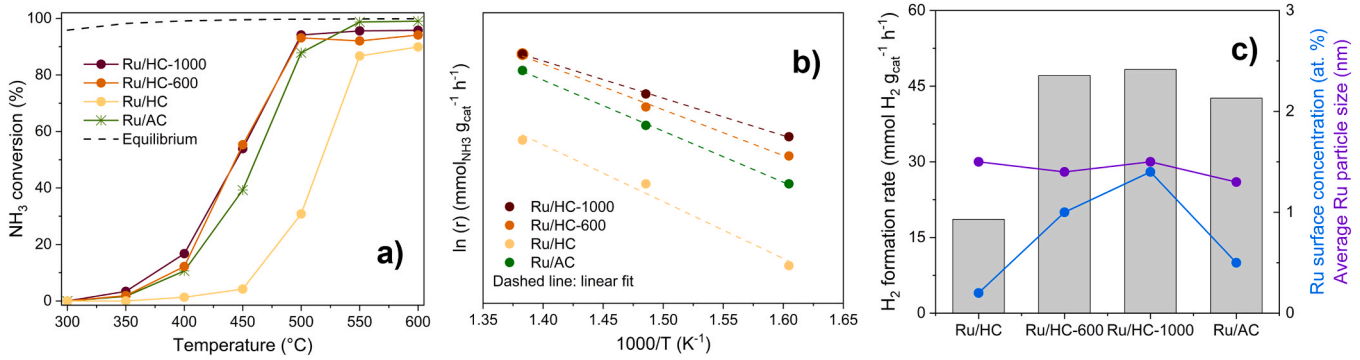

Fig. 7. a) NH_3 conversion of Ru catalysts including the thermodynamic equilibrium (dashed) and the reference material (Ru/AC), measured with the standard protocol. b) The Arrhenius plots of the Ru catalysts calculated at the temperatures 350 °C, 400 °C and 450 °C. c) The H_2 formation rates of the catalysts of this study from a) at 450 °C with the Ru surface concentration from XPS of the reduced catalysts in at% and average Ru particle size in nm from STEM.

Throughout the studied temperature range, the thermodynamic equilibrium was calculated to be close to full conversion with a slight increase at 300 °C to 450 °C from 95.7 % to 99.7 %. Among the catalysts tested, Ru/HC exhibited the lowest overall activity throughout the entire temperature range, achieving a conversion of only 4.0 % at 450 °C and 30.3 % at 500 °C. Thus, untreated HC was found to be unsuitable as a support for Ru, presumably due to its predominantly amorphous structure and low degree of graphitization, as evidenced by Raman (Fig. 2) and XRD (Figure S4). Additionally, the decomposition of less stable nitrogen species, such as amine N, during calcination and reduction may negatively impact metal distribution, as evidenced by STEM analysis (Fig. 4a)). In contrast, both Ru/HC-600 and Ru/HC-1000 exhibited an improved NH_3 conversion, achieving 55.1 % and 53.7 % at 450 °C, respectively, and over 90 % conversion at 500 °C. For HC-600, a decline in conversion was observed between 500 °C and 600 °C, whereas for HC-1000 the level of conversion remained constant. The XRD data illustrated an increase in the degree of graphitization with higher pyrolysis temperatures, enhancing the structural integrity of the catalyst and ensuring consistent catalytic performance during ammonia decomposition. The average Ru particle size of the reduced catalysts, measured before testing, was comparably low (1.3 nm to 1.5 nm; Fig. 4, Table 1) for all catalysts, indicating that particle size does not significantly impact catalytic performance. On the contrary, the reference catalyst, Ru/AC, demonstrated a lower activity at temperatures < 550 °C, with conversions of about 39.4 % and 87.7 % at 450 °C and 500 °C, respectively.

For all catalysts analyzed in this study, an increase of the masses 15 and 16 was qualitatively observed at T > 520 °C by the mass spectrometer analyzing the product gas, indicating the formation of methane as a result of Ru-assisted support decomposition (Figure S11). Additional measurements using an FTIR to quantify methane formation were unsuccessful, as the detected levels were below the 20-ppm detection limit. Yet, it's unclear why the conversion drop can be only observed for HC-600. Thus, these points should be addressed further in future studies.

The apparent activation energy (E_a) can be determined using the Arrhenius equation by fitting it to the reaction rate data as a function of the inverse reaction temperature, as illustrated in Fig. 7b): Ru/HC-1000 < Ru/HC-600 < Ru/AC < Ru/HC. The lower activation energy observed for the HC-derived and pyrolyzed catalysts may arise from the additional interaction between Ru and nitrogen functionalities in the carbon support, as discussed in chapter 3.2. The stronger Ru-support interaction (as evidenced by H_2-TPR) facilitates N–H bond cleavage, one rate-determining step in ammonia decomposition [17]. In contrast, Ru on conventional activated carbon lacks such stabilizing interactions, leading to higher activation barriers.

The dependency of the H_2 formation rate on the average Ru particle size and Ru surface concentration is demonstrated in Fig. 7c). We can conclude that the H_2 formation rate does not depend on the average Ru particle size, but it depends on the Ru surface concentration, which is the lowest for Ru/HC with 0.2 at%.

To enable a quantitative comparison of catalytic activity, a reference temperature of 450 °C was selected. Fig. 8a) displays the NH_3 conversion at this temperature over 16 h, measured using the same activation procedure as in Fig. 7a). The Ru/HC-600 catalyst exhibited a significant increase in conversion of 34.2 % during this period, while Ru/HC-1000 demonstrated a modest linear increase of only 4.9 %. Notably, after 16 h, the NH_3 conversion of Ru/HC-600 surpassed that of Ru/HC-1000 by 10 %. The interaction between Ru and the support material is influenced by the specific nature of the surface functional groups present on the support. Variations in these surface groups can lead to differing anchoring mechanisms, which in turn affect the stability of Ru species. On the HC-600 support, the probability of Ru anchoring on oxygen species is increased due to the greater availability of such sites (Table S5 and S7), which aligns with the first reduction peak shift towards higher temperatures in the H_2-TPR profiles (Fig. 5). This stronger interaction may inhibit the complete crystallization of Ru atoms during catalyst preparation and activation, resulting in a partially amorphous state.

Fig. 4e)-f) shows the state of the Ru nanoparticles embedded in 600

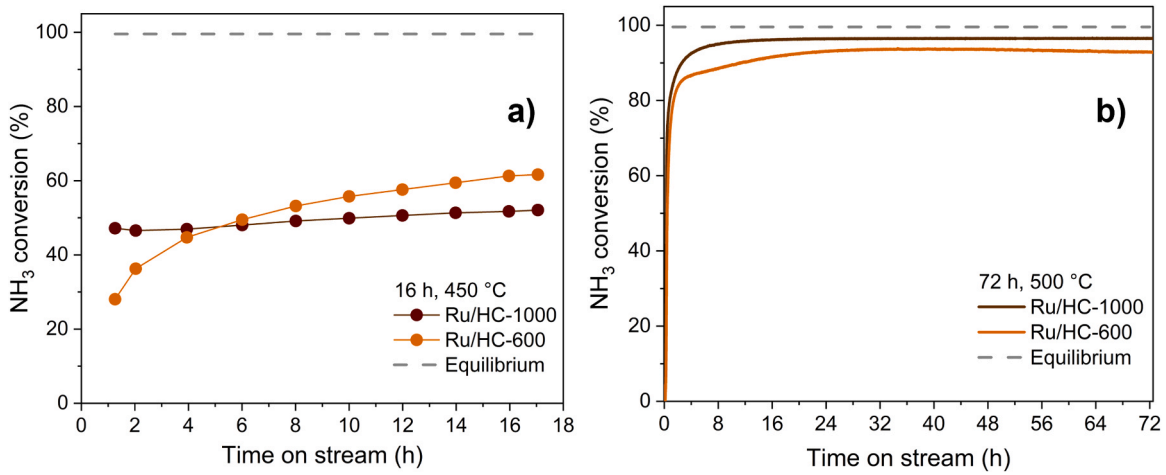

Fig. 8. a) NH_3 conversion of the HC-derived catalysts at 450 °C for 16 h, and b) at 500 °C for 72 h.

ºC and 1000 ºC pyrolyzed carbon support after sustaining 16 h in NH_3 decomposition. While the particle distribution inside the support looked identical for both samples, observable differences in the crystalline quality and size distribution can be observed. In terms of crystallinity, the nanoparticles in 600 ºC pyrolyzed sample showed a more distorted appearance compared to the 1000 ºC (insets, Figure S6). Additionally, the average particle size after NH_3 conversion increased for both samples from 1.4/1.5–2.3/2.9 nm respectively, indicating some restructuring of the Ru morphology during the catalytic reaction. These nano structural variations could be related to the differences in NH_3 conversion rate between the pyrolyzed samples in Fig. 8).

Finally, a long-term conversion experiment was conducted, shown in Fig. 8b). The measurements were carried out for 72 h at 500 °C to evaluate the stability in terms of mass loss of the catalyst. The Ru/HC-1000 catalyst achieved a conversion rate of 96.6 % after 8 h and maintained this stability for the subsequent 64 h. The Ru/HC-600 catalyst reached a plateau at 93.5 % conversion after 24 h, showing a slight decline of 0.7 % towards the end. The total mass loss, including the catalyst's activation, was 12 % for Ru/HC-1000 and 46 % for Ru/HC-600. This finding indicates that the higher pyrolyzed hydrochar is more stable under those reaction conditions. No clear difference in particle size or distribution was observed in post-reaction STEM analysis, although a marginally higher particle density could be apparent per square area in Ru/HC-1000 compared Ru/HC600 (Figure S8).

In Table 3, the catalysts synthesized in this study are compared with selected carbon-based Ru catalysts from the literature. The HC-derived catalysts not only demonstrate good potential but also compete effectively with other state-of-the-art Ru catalysts in terms of catalytic performance at 450 °C, despite their comparatively low loadings. Furthermore, the positive impact of nitrogen surface groups on carbon supports applies not only to our HC supports but also to other materials reported in the literature, such as CNTs, CNFs, and OMC (ordered mesoporous carbon) (see Table 3).

4. Conclusion

In this study, hydrochar and pyrolyzed hydrochar were evaluated as potential supports for Ru catalysts in NH_3 decomposition. The carbon supports were synthesized via HTC and subsequent pyrolysis of chitosan, successfully incorporating nitrogen into the carbon matrix. XPS demonstrated the removal of oxygen-containing functional groups and a decreasing O-to-N ratio (from 7 to 1.3) through pyrolysis. The nitrogen content remained stable from HC to HC-600 but diminished in HC-1000. XPS analysis indicated that HC contained only pyrrolic and amine nitrogen, with the latter decreasing post-pyrolysis and transforming into pyridinic and quaternary nitrogen. For a nitrogen-free comparison, commercial activated carbon was used.

All catalysts used within this study were loaded with 1 wt% Ru. STEM analysis revealed a consistent average Ru size ranging from 1.3 nm to 1.5 nm across all catalysts, including the Ru/AC reference. This consistency suggests that support functionalization does not significantly affect Ru particle size. However, the pyrolysis step is essential for achieving a homogeneous Ru metal distribution. This requirement is reflected in the catalytic activity during NH_3 decomposition, where pyrolyzed hydrochar catalysts exhibited a 14-fold increase in conversion compared to non-pyrolyzed hydrochar and superior activity compared to Ru/AC at temperatures $\leq$ 500 °C. The activation energies increased in the order: Ru/HC-1000 < Ru/HC-600 < Ru/AC

Table 3
Comparison of different carbon-based Ru catalysts in ammonia decomposition.

Sample	Ru loading (wt%)	Feed gas	WHSV ($ml_N\ g_{cat}^{-1}\ h^{-1}$)	Temperature (°C)	NH_3 conversion (%)	E_a (kJ mol^{-1})	Reference
Ru/HC	0.9	5 % NH_3 in He	15 000	450	4.0	130.2	This study
Ru/HC−600	1.1	5 % NH_3 in He	15 000	450	56.0	104.7	This study
Ru/HC−1000	1.2	5 % NH_3 in He	15 000	450	54.0	85.3	This study
Ru/AC	1.0	5 % NH_3 in He	15 000	450	39.0	116.8	This study
Ru/AC	4.8	100 % NH_3	30 000	450	9.6	85.9	[33]
Ru/CNTs	4.8	100 % NH_3	30 000	450	14.5	89.4	[33]
Ru/CNTs	2.0	10 % NH_3 in Ar	20 000	450	42.0	n.a.	[89]
Ru/N-CNTs	2.0	10 % NH_3 in Ar	20 000	450	65.0	n.a.	[89]
Ru/CNFs	3.9	5 % NH_3 in Ar	9 900	450	72.1	n.a.	[43]
Ru/N-CNFs	5.1	5 % NH_3 in Ar	9 900	450	86.4	n.a.	[43]
Ru/O-CNFs	3.7	5 % NH_3 in Ar	9900	450	69.0	n.a.	[43]
Ru/OMC	5.0	100 % NH_3	6000	450	59.0	> 37	[79]
Ru/N-OMC	5.0	100 % NH_3	6000	450	85.0	37	[79]

< Ru/HC, ranging from 85 kJ mol^{-1} for Ru/HC-1000–130 kJ mol^{-1} for Ru/HC. Consistent with the literature, the presence of nitrogen is believed to enhance the electronic properties of the hydrochar-derived catalysts, as evidenced by XPS revealing the Ru-N interaction in Ru/HC-1000. This interaction was absent in Ru/HC and Ru/HC-600, likely due to their higher oxygen content. Furthermore, XRD analysis indicates that the enhanced graphitization resulting from pyrolysis favorably influences the dispersion of metal particles.

Following NH_3 decomposition, the average Ru size increased for both Ru/HC-600 and Ru/HC-1000, measuring 2.3 nm and 2.9 nm, respectively, after 16 h at 450 °C. This size evolution is presumably influenced by the supports' surface chemistry, with recrystallization processes more pronounced in Ru/HC-600, leading to enhanced conversion rates at 450 °C.

Long-term stability tests revealed that the Ru/HC-1000 catalyst exhibited a better mass loss resistance and consistent catalytic activity over 72 h at 500 °C without methane formation. Methane formation was qualitatively detected via mass spectrometry for all catalysts, starting at 520 °C.

Pyrolyzed hydrochar is a promising support for Ru in NH_3 decomposition, allowing for adjustable surface functionalization. Future research will aim to enhance the reactivity and stability of Ru nanoparticles during ammonia decomposition by integrating various promoters into the catalytic system.

CRediT authorship contribution statement

Miranda Guci: Writing – review & editing, Writing – original draft, Visualization, Methodology, Investigation, Formal analysis, Conceptualization. **Markus Knäbbeler-Buß:** Writing – review & editing, Supervision, Methodology, Conceptualization. **Emma Verkama:** Writing – review & editing, Methodology. **Michael Günthel:** Writing – review & editing, Investigation, Formal analysis. **Md Redwanul Islam:** Writing – review & editing, Investigation, Formal analysis. **Lorenz Kienle:** Writing – review & editing, Conceptualization. **Erisa Saraçi:** Writing – review & editing, Supervision, Conceptualization. **Jan-Dierk Grunwaldt:** Writing – review & editing, Supervision, Conceptualization. **Florian Nestler:** Writing – review & editing, Supervision, Methodology, Conceptualization.

Funding

The authors sincerely thank the German Federal Ministry of Research, Technology and Space (BMFTR) for funding this work as part of the AmmoCatCoat project (grant number: 03XP0613B).

Declaration of Competing Interest

The authors declare that they have no known competing financial interests or personal relationships that could have appeared to influence the work reported in this paper.

Acknowledgments

We express our gratitude to all project partners of the AmmoCatCoat project for their valuable contributions to this research. We also wish to thank Florian Maurer from the Karlsruhe Institute of Technology for his assistance with the graphical abstract.

Appendix A. Supporting information

Supplementary data associated with this article can be found in the online version at doi:10.1016/j.apcata.2025.120616.

Data availability

Data will be made available on request.

References

[1] S.E. Hosseini, M.A. Wahid, Hydrogen production from renewable and sustainable energy resources: promising Green energy carrier for clean development, Renew. Sustain. Energy Rev. 57 (2016) 850–866, https://doi.org/10.1016/j.rser.2015.12.112.
[2] K.T. Møller, T.R. Jensen, E. Akiba, H. Li, Hydrogen - a sustainable energy carrier, *Prog. Nat. Sci. Mater. Int.* 27 (2017) 34–40, https://doi.org/10.1016/j.pnsc.2016.12.014.
[3] J.O. Abe, A. Popoola, E. Ajenifuja, O.M. Popoola, Hydrogen energy, economy and storage: review and recommendation, Int. J. Hydrog. Energy 44 (2019) 15072–15086, https://doi.org/10.1016/j.ijhydene.2019.04.068.
[4] F. Dawood, M. Anda, G.M. Shafiullah, Hydrogen production for energy: an overview, Int. J. Hydrog. Energy 45 (2020) 3847–3869, https://doi.org/10.1016/j.ijhydene.2019.12.059.
[5] E. Pawelczyk, N. Łukasik, I. Wysocka, A. Rogala, J. Gębicki, Recent progress on hydrogen storage and production using chemical hydrogen carriers, Energies 15 (2022) 4964, https://doi.org/10.3390/en15144964.
[6] J. Andersson, S. Grönkvist, Large-scale storage of hydrogen, Int. J. Hydrog. Energy 44 (2019) 11901–11919, https://doi.org/10.1016/j.ijhydene.2019.03.063.
[7] T. He, P. Pachfule, H. Wu, Q. Xu, P. Chen, Hydrogen carriers, Nat. Rev. Mater. 1 (2016), https://doi.org/10.1038/natrevmats.2016.59.
[8] P. Schühle, R. Stöber, M. Gierse, A. Schaadt, R. Szolak, S. Thill, M. Alders, C. Hebling, P. Wasserscheid, O. Salem, Dimethyl ether/CO 2 – a hitherto underestimated h 2 storage cycle, Energy Environ. Sci. 16 (2023) 3002–3013, https://doi.org/10.1039/D3EE00228D.
[9] A. Banu, Y. Bicer, Integration of methane cracking and direct carbon fuel cell with CO2 capture for hydrogen carrier production, Int. J. Hydrog. Energy 47 (2022) 19502–19516, https://doi.org/10.1016/j.ijhydene.2022.04.187.
[10] H. Jorschick, M. Geißelbrecht, M. Eßl, P. Preuster, A. Bösmann, P. Wasserscheid, Benzyltoluene/dibenzyltoluene-based mixtures as suitable liquid organic hydrogen carrier systems for low temperature applications, Int. J. Hydrog. Energy 45 (2020) 14897–14906, https://doi.org/10.1016/j.ijhydene.2020.03.210.
[11] S. Sun, Q. Jiang, D. Zhao, T. Cao, H. Sha, C. Zhang, H. Song, Z. Da, Ammonia as hydrogen carrier: advances in ammonia decomposition catalysts for promising hydrogen production, Renew. Sustain. Energy Rev. 169 (2022) 112918, https://doi.org/10.1016/j.rser.2022.112918.
[12] H. Nozari, A. Karabeyoğlu, Numerical study of combustion characteristics of ammonia as a renewable fuel and establishment of reduced reaction mechanisms, Fuel 159 (2015) 223–233, https://doi.org/10.1016/j.fuel.2015.06.075.
[13] A. Valera-Medina, H. Xiao, M. Owen-Jones, W. David, P.J. Bowen, Ammonia for power, Prog. Energy Combust. Sci. 69 (2018) 63–102, https://doi.org/10.1016/j.pecs.2018.07.001.
[14] R. Schlögl. Ammonia Synthesis, in Handbook of HeterogeneousCatalysis, in 2, ed., Wiley-VCH, Weinheim, 2008.
[15] Elie Bellevrat, Kira West, Clean and efficient heat for industry.
[16] S. Mukherjee, S.V. Devaguptapu, A. Sviripa, C.R. Lund, G. Wu, Low-temperature ammonia decomposition catalysts for hydrogen generation, Appl. Catal. B Environ. 226 (2018) 162–181, https://doi.org/10.1016/j.apcatb.2017.12.039.
[17] J.C. Ganley, F.S. Thomas, E.G. Seebauer, R.I. Masel, A priori catalytic activity correlations: the difficult case of hydrogen production from ammonia, Catal. Lett. 96 (2004) 117–122, https://doi.org/10.1023/B:CATL.0000030108.50691.d4.
[18] A.J. Medford, A. Vojvodic, J.S. Hummelshøj, J. Voss, F. Abild-Pedersen, F. Studt, T. Bligaard, A. Nilsson, J.K. Nørskov, From the sabatier principle to a predictive theory of transition-metal heterogeneous catalysis, J. Catal. 328 (2015) 36–42, https://doi.org/10.1016/j.jcat.2014.12.033.
[19] A. BOISEN, S. DAHL, J. NORSKOV, C. CHRISTENSEN, Why the optimal ammonia synthesis catalyst is not the optimal ammonia decomposition catalyst, J. Catal. 230 (2005) 309–312, https://doi.org/10.1016/j.jcat.2004.12.013.
[20] W. Arabczyk, J. Zamlynny, Study of the ammonia decomposition over iron catalysts, Catal. Lett. 60 (1999) 167–171, https://doi.org/10.1023/A:1019007024041.
[21] F.R. García-García, A. Guerrero-Ruiz, I. Rodríguez-Ramos, Role of B5-Type sites in ru catalysts used for the NH3 decomposition reaction, Top. Catal. 52 (2009) 758–764, https://doi.org/10.1007/s11244-009-9203-7.
[22] I. Chorkendorff, Concepts of Modern Catalysis and Kinetics, WILEY-VCH, Weinheim, 2003.
[23] H. Yuzawa, T. Mori, H. Itoh, H. Yoshida, Reaction mechanism of ammonia decomposition to nitrogen and hydrogen over metal loaded titanium oxide photocatalyst, J. Phys. Chem. C 116 (2012) 4126–4136, https://doi.org/10.1021/jp209795t.
[24] M. Itoh, M. Masuda, K. Machida, Hydrogen generation by ammonia cracking with iron Metal-Rare earth oxide composite catalyst, Mater. Trans. 43 (2002) 2763–2767, https://doi.org/10.2320/matertrans.43.2763.
[25] H. Yan, Y.-J. Xu, Y.-Q. Gu, H. Li, X. Wang, Z. Jin, S. Shi, R. Si, C.-J. Jia, C.-H. Yan, Promoted multimetal oxide catalysts for the generation of hydrogen via ammonia decomposition, J. Phys. Chem. C 120 (2016) 7685–7696, https://doi.org/10.1021/acs.jpcc.6b01595.

[26] M. Nishi, S.-Y. Chen, T. Mochizuki, The role of carbon supports for Ru-based catalysts in ammonia decomposition: a review, Carbon Rep. 3 (2024) 2–10, https://doi.org/10.7209/carbon.030105.
[27] A. Rendon-Patiño, D. Mateo, S. Duran-Uribe, A. Sepulveda-Escribano, J. Gascon, E. V. Ramos-Fernandez, Ruthenium Nanoparticles within Carbon Spheres for Efficient Ammonia Decomposition, ChemCatChem. https://doi.org/10.1002/cctc.202400878.
[28] S. Basu-Dutt, M.L. Minus, R. Jain, D. Nepal, S. Kumar, Chemistry of carbon nanotubes for everyone, J. Chem. Educ. 89 (2012) 221–229, https://doi.org/10.1021/ed1005163.
[29] M. Guler, C. Korkusuz, D. Varisli, Catalytic decomposition of ammonia for hydrogen production over carbon nanofiber supported fe and mo catalysts in a microwave heated reactor, Int. J. Chem. React. Eng. 17 (2019), https://doi.org/10.1515/ijcre-2018-0162.
[30] S. Mazzone, T. Goklany, G. Zhang, J. Tan, E.I. Papaioannou, F.R. García-García, Ruthenium-based catalysts supported on carbon xerogels for hydrogen production via ammonia decomposition, Appl. Catal. A Gen. 632 (2022) 118484, https://doi.org/10.1016/j.apcata.2022.118484.
[31] L. Li, Q. Meng, W. Ji, J. Shao, Q. Xu, J. Yan, Embedded iron nanoparticles by graphitized carbon as highly active yet stable catalyst for ammonia decomposition, Mol. Catal. 442 (2017) 147–153, https://doi.org/10.1016/j.mcat.2017.09.013.
[32] L. Li, F. Chen, Y. Dai, J. Wu, J.L. Shao, H.Y. Li, Fe-assisted ru clusters supported on porous and graphitic carbon for ammonia decomposition to CO x free hydrogen, RSC Adv. 6 (2016) 102336–102342, https://doi.org/10.1039/C6RA21211E.
[33] S.F. Yin, B.Q. Xu, W.X. Zhu, C.F. Ng, X.P. Zhou, C.T. Au, Carbon nanotubes-supported ru catalyst for the generation of COx-free hydrogen from ammonia, Catal. Today 93-95 (2004) 27–38, https://doi.org/10.1016/j.cattod.2004.05.011.
[34] S.-F. Yin, B.-Q. Xu, C.-F. Ng, C.-T. Au, Nano Ru/CNTs: a highly active and stable catalyst for the generation of CO -free hydrogen in ammonia decomposition, Appl. Catal. B Environ. 48 (2004) 237–241, https://doi.org/10.1016/j.apcatb.2003.10.013.
[35] S.-F. Yin, Q.-H. Zhang, B.-Q. Xu, W.-X. Zhu, C.-F. Ng, C.-T. Au, Investigation on the catalysis of COx-free hydrogen generation from ammonia, J. Catal. 224 (2004) 384–396, https://doi.org/10.1016/j.jcat.2004.03.008.
[36] Xuezhi Duan, Jinghong ZHOU, Gang Qian, Ping L.I., Xinggui Zhou, De Chen, Carbon Nanofiber-Supported Ru Catalysts for Hydrogen Evolution by Ammonia Decomposition.
[37] R. Shoukat, M.I. Khan, Carbon nanotubes/nanofibers (CNTs/CNFs): a review on state of the art synthesis methods, Micro Technol. 28 (2022) 885–901, https://doi.org/10.1007/s00542-022-05263-2.
[38] J. Chen, Z.H. Zhu, S. Wang, Q. Ma, V. Rudolph, G.Q. Lu, Effects of nitrogen doping on the structure of carbon nanotubes (CNTs) and activity of Ru/CNTs in ammonia decomposition, Chem. Eng. J. 156 (2010) 404–410, https://doi.org/10.1016/j.cej.2009.10.062.
[39] S. Ren, F. Huang, J. Zheng, S. Chen, H. Zhang, Ruthenium supported on nitrogen-doped ordered mesoporous carbon as highly active catalyst for NH3 decomposition to H2, Int. J. Hydrog. Energy 42 (2017) 5105–5113, https://doi.org/10.1016/j.ijhydene.2016.11.010.
[40] L.F. Mabena, S. Sinha Ray, S.D. Mhlanga, N.J. Coville, Nitrogen-doped carbon nanotubes as a metal catalyst support, Appl. Nanosci. 1 (2011) 67–77, https://doi.org/10.1007/s13204-011-0013-4.
[41] Hua Wang, Caili Xu, Qian Chen, Mei Ming, Yi Wang, Ting Sun, Yun Zhang, Daojiang Gao, Jian Bi, and Guangyin Fan, Nitrogen-Doped Carbon Stabilized Ru Nanoclusters as Excellent Catalyst for Hydrogen Production.
[42] F.R. García-García, M. Fernández-García, M.A. Newton, I. Rodríguez-Ramos, A. Guerrero-Ruiz, Following the evolution of Ru/Activated carbon catalysts during the Decomposition–Reduction of the Ru(NO)(NO 3) 3 precursor, ChemCatChem 5 (2013) 2446–2452, https://doi.org/10.1002/cctc.201300065.
[43] Y. Marco, L. Roldán, S. Armenise, E. García-Bordejé, Support-Induced oxidation state of catalytic ru nanoparticles on carbon nanofibers that were doped with heteroatoms (O, N) for the decomposition of NH3 // Support-Induced oxidation state of catalytic ru nanoparticles on carbon nanofibers that were doped with heteroatoms (O, N) for the decomposition of NH 3, ChemCatChem 5 (2013) 3829–3834, https://doi.org/10.1002/cctc.201300455.
[44] J. Chen, Z.H. Zhu, S. Wang, Q. Ma, V. Rudolph, G.Q. Lu, Effects of nitrogen doping on the structure of carbon nanotubes (CNTs) and activity of Ru/CNTs in ammonia decomposition, Chem. Eng. J. 156 (2010) 404–410, https://doi.org/10.1016/j.cej.2009.10.062.
[45] N. Job, A. Théry, R. Pirard, J. Marien, L. Kocon, J.-N. Rouzaud, F. Béguin, J.-P. Pirard, Carbon aerogels, cryogels and xerogels: influence of the drying method on the textural properties of porous carbon materials, Carbon 43 (2005) 2481–2494, https://doi.org/10.1016/j.carbon.2005.04.031.
[46] J.W. Straten, P. Schleker, M. Krasowska, E. Veroutis, J. Granwehr, A.A. Auer, W. Hetaba, S. Becker, R. Schlögl, S. Heumann, Nitrogen-functionalized hydrothermal carbon materials by using urotropine as the nitrogen precursor, Chemistry 24 (2018) 12298–12317, https://doi.org/10.1002/chem.201800341.
[47] A.J. Ramiro de Castro, G.D. Saraiva, A.C. Oliveira, V.O. Sousa Neto, A.J. Paula, A. G. Souza Filho, O.P. Ferreira, Ordered porous carbons from hydrothermally treated biomass: effects of the thermal treatments on the structure and porosity, Vib. Spectrosc. 111 (2020) 103175, https://doi.org/10.1016/j.vibspec.2020.103175.
[48] M.-M. Titirici, R.J. White, C. Falco, M. Sevilla, Black perspectives for a Green future: hydrothermal carbons for environment protection and energy storage, Energy Environ. Sci. 5 (2012) 6796, https://doi.org/10.1039/c2ee21166a.
[49] N. Hammi, S. Chen, F. Dumeignil, S. Royer, A. El Kadib, Chitosan as a sustainable precursor for nitrogen-containing carbon nanomaterials: synthesis and uses, Mater. Today Sustain. 10 (2020) 100053, https://doi.org/10.1016/j.mtsust.2020.100053.
[50] H. Ababneh, B.H. Hameed, Chitosan-derived hydrothermally carbonized materials and its applications: a review of recent literature, Int. J. Biol. Macromol. 186 (2021) 314–327, https://doi.org/10.1016/j.ijbiomac.2021.06.161.
[51] J. Wang, S. Chen, J. Xu, L. Liu, J. Zhou, J. Cai, High-surface-area porous carbons produced by the mild KOH activation of a chitosan hydrochar and their CO2 capture, N. Carbon Mater. 36 (2021) 1081–1090, https://doi.org/10.1016/S1872-5805(21)60074-4.
[52] Á. Molnár, The use of chitosan-based metal catalysts in organic transformations, Coord. Chem. Rev. 388 (2019) 126–171, https://doi.org/10.1016/j.ccr.2019.02.018.
[53] J. Ding, L. Zhong, Q. Huang, Y. Guo, T. Miao, Y. Hu, J. Qian, S. Huang, Chitosan hydrogel derived carbon foam with typical transition-metal catalysts for efficient water splitting, Carbon 177 (2021) 160–170, https://doi.org/10.1016/j.carbon.2021.01.160.
[54] M. Rinaudo, Chitin and chitosan: properties and applications, Prog. Polym. Sci. 31 (2006) 603–632, https://doi.org/10.1016/j.progpolymsci.2006.06.001.
[55] D. Pauly, R. Froese, Comments on FAO's state of fisheries and aquaculture, or 'Sofia 2010, Mar. Policy 36 (2012) 746–752, https://doi.org/10.1016/j.marpol.2011.10.021.
[56] A.M. Smith, S. Singh, A.B. Ross, Fate of inorganic material during hydrothermal carbonisation of biomass: influence of feedstock on combustion behaviour of hydrochar, Fuel 169 (2016) 135–145, https://doi.org/10.1016/j.fuel.2015.12.006.
[57] M.T. Reza, J.G. Lynam, M.H. Uddin, C.J. Coronella, Hydrothermal carbonization: fate of inorganics, Biomass Bioenergy 49 (2013) 86–94, https://doi.org/10.1016/j.biombioe.2012.12.004.
[58] S. Brunauer, P.H. Emmett, E. Teller, Adsorption of gases in multimolecular layers, J. Am. Chem. Soc. 60 (1938) 309–319, https://doi.org/10.1021/ja01269a023.
[59] G.Y. Gor, M. Thommes, K.A. Cychosz, A.V. Neimark, Quenched solid density functional theory method for characterization of mesoporous carbons by nitrogen adsorption, Carbon 50 (2012) 1583–1590, https://doi.org/10.1016/j.carbon.2011.11.037.
[60] O.A. Ojelade, S.F. Zaman, Ammonia decomposition for hydrogen production: a thermodynamic study, Chem. Pap. 75 (2021) 57–65, https://doi.org/10.1007/s11696-020-01278-z.
[61] M.-M. Titirici, M. Antonietti, Chemistry and materials options of sustainable carbon materials made by hydrothermal carbonization, Chem. Soc. Rev. 39 (2010) 103–116, https://doi.org/10.1039/b819318p.
[62] H. Simsir, N. Eltugral, S. Karagoz, Hydrothermal carbonization for the preparation of hydrochars from glucose, cellulose, chitin, chitosan and wood chips via low-temperature and their characterization, Bioresour. Technol. 246 (2017) 82–87, https://doi.org/10.1016/j.biortech.2017.07.018.
[63] M. Bengisu, E. Yilmaz, Oxidation and pyrolysis of chitosan as a route for carbon fiber derivation, Carbohydr. Polym. 50 (2002) 165–175, https://doi.org/10.1016/S0144-8617(02)00018-8.
[64] M. Mäkelä, A. Fullana, K. Yoshikawa, Ash behavior during hydrothermal treatment for solid fuel applications. Part 1: overview of different feedstock, Energy Convers. Manag. 121 (2016) 402–408, https://doi.org/10.1016/j.enconman.2016.05.016.
[65] K.S.W. Sing, D.H. Everett, R.A.W. Haul, L. Moscou, R.A. Pierotti, J. Rouquerol, T. Siemieniewska (Eds.), Reporting Physisorption Data for Gas/Solid Systems, 2nd ed., WILEY-VCH, Weinheim, 2008.
[66] K. Sing, The use of nitrogen adsorption for the characterisation of porous materials, Colloids Surf. A Physicochem. Eng. Asp. 187-188 (2001) 3–9, https://doi.org/10.1016/S0927-7757(01)00612-4.
[67] A.J.R. Castro, G.D. Saraiva, A.C. Oliveira, V.O.S. Neto, F.H. Soares, L.H.S. Vieira, A. G.S. Filho, O.P. Ferreira, Synthesis and detailed characterization of hydrochars and biochars from chitosan, Biomass. Conv. Bioref. 15 (2025) 14123–14136, https://doi.org/10.1007/s13399-024-06270-1.
[68] Z.Q. Li, C.J. Lu, Z.P. Xia, Y. Zhou, Z. Luo, X-ray diffraction patterns of graphite and turbostratic carbon, Carbon 45 (2007) 1686–1695, https://doi.org/10.1016/j.carbon.2007.03.038.
[69] P. Puech, A. Dabrowska, N. Ratel-Ramond, G.L. Vignoles, M. Monthioux, New insight on carbonisation and graphitisation mechanisms as obtained from a bottom-up analytical approach of X-ray diffraction patterns, Carbon 147 (2019) 602–611, https://doi.org/10.1016/j.carbon.2019.03.013.
[70] P. Serp, J.L. Figueiredo, Carbon Materials for Catalysis, Wiley, Hoboken, N.J, 2008.
[71] L. Leng, L. Yang, S. Leng, W. Zhang, Y. Zhou, H. Peng, H. Li, Y. Hu, S. Jiang, H. Li, A review on nitrogen transformation in hydrochar during hydrothermal carbonization of biomass containing nitrogen, Sci. Total Environ. 756 (2021) 143679, https://doi.org/10.1016/j.scitotenv.2020.143679.
[72] L. Leng, S. Xu, R. Liu, T. Yu, X. Zhuo, S. Leng, Q. Xiong, H. Huang, Nitrogen containing functional groups of biochar: an overview, Bioresour. Technol. 298 (2020) 122286, https://doi.org/10.1016/j.biortech.2019.122286.
[73] M. Ayiania, M. Smith, A.J. Hensley, L. Scudiero, J.-S. McEwen, M. Garcia-Perez, Deconvoluting the XPS spectra for nitrogen-doped chars: an analysis from first principles, Carbon 162 (2020) 528–544, https://doi.org/10.1016/j.carbon.2020.02.065.
[74] M. Bosilj, L. Rustam, R. Thomann, J. Melke, A. Fischer, R.J. White, Directing nitrogen-doped carbon support chemistry for improved aqueous phase hydrogenation catalysis, Catal. Sci. Technol. 10 (2020) 4794–4808, https://doi.org/10.1039/D0CY00391C.
[75] Z. Huang, Z. Liao, W. Yang, H. Zhou, C. Fu, Y. Gong, L. Chen, Y. Kuang, Different types of nitrogen species in nitrogen-doped carbon material: the formation mechanism and catalytic role on oxygen reduction reaction, Electrochim. Acta 245 (2017) 957–966, https://doi.org/10.1016/j.electacta.2017.06.026.
[76] S. Xu, J. Chen, H. Peng, S. Leng, H. Li, W. Qu, Y. Hu, H. Li, S. Jiang, W. Zhou, L. Leng, Effect of biomass type and pyrolysis temperature on nitrogen in biochar,

and the comparison with hydrochar, Fuel 291 (2021) 120128, https://doi.org/10.1016/j.fuel.2021.120128.
[77] Li Zhao, Niki Baccile, Silvia Gross, Yuanjian Zhang, Wei Wei, Yuhan Sun, Markus Antonietti, Maria-Magdalena Titirici, Sustainable nitrogen-doped carbonaceous materials from biomass derivatives.
[78] D. Ye, K.C. Leung, W. Niu, M. Duan, J. Li, P.-L. Ho, D. Szalay, T.-S. Wu, Y.-L. Soo, S. Wu, S.C.E. Tsang, Active nitrogen sites on nitrogen doped carbon for highly efficient associative ammonia decomposition, iScience 27 (2024) 110571, https://doi.org/10.1016/j.isci.2024.110571.
[79] S. Ren, F. Huang, J. Zheng, S. Chen, H. Zhang, Ruthenium supported on nitrogen-doped ordered mesoporous carbon as highly active catalyst for NH3 decomposition to H2, Int. J. Hydrog. Energy 42 (2017) 5105–5113, https://doi.org/10.1016/j.ijhydene.2016.11.010.
[80] L. Li, Z.H. Zhu, Z.F. Yan, G.Q. Lu, L. Rintoul, Catalytic ammonia decomposition over ru/carbon catalysts: the importance of the structure of carbon support, Appl. Catal. A Gen. 320 (2007) 166–172, https://doi.org/10.1016/j.apcata.2007.01.029.
[81] Y. Xu, Y. Wang, C. Wu, H. Huang, Y. Zhang, J. Nan, H. Yu, Y. Zhao, Structure effect of activated carbon in Ru/AC catalysts for hydrogenation of phthalates, Catal. Commun. 132 (2019) 105825, https://doi.org/10.1016/j.catcom.2019.105825.
[82] Z. Kowalczyk, J. Sentek, S. Jodzis, E. Mizera, J. Góralski, T. Paryjczak, R. Diduszko, An alkali-promoted ruthenium catalyst for the synthesis of ammonia, supported on thermally modified active carbon, Catal. Lett. 45 (1997) 65–72, https://doi.org/10.1023/A:1018970318628.
[83] L. Forni, D. Molinari, I. Rossetti, N. Pernicone, Carbon-supported promoted ru catalyst for ammonia synthesis, Appl. Catal. A Gen. 185 (1999) 269–275, https://doi.org/10.1016/S0926-860X(99)00144-1.
[84] D.J. Morgan, Resolving ruthenium: XPS studies of common ruthenium materials, Surf. Interface Anal. 47 (2015) 1072–1079, https://doi.org/10.1002/sia.5852.
[85] Y. Lee, J.H. Ahn, S. Shin, S.-H. Jung, H.-S. Park, Y.-G. Cho, D.-G. Lee, H. Kong, J. H. Lee, H.-K. Song, Metal-nitrogen intimacy of the nitrogen-doped ruthenium oxide for facilitating electrochemical hydrogen production, Appl. Catal. B Environ. 303 (2022) 120873, https://doi.org/10.1016/j.apcatb.2021.120873.
[86] S. Armenise, L. Roldán, Y. Marco, A. Monzón, E. García-Bordejé, Elucidation of catalyst support effect for NH3 decomposition using ru nanoparticles on Nitrogen-Functionalized carbon nanofiber monoliths // elucidation of catalyst support effect for NH 3 decomposition using ru nanoparticles on Nitrogen-Functionalized carbon nanofiber monoliths, J. Phys. Chem. C. 116 (2012) 26385–26395, https://doi.org/10.1021/jp308985x.
[87] H. Clavier, J.L. Petersen, S.P. Nolan, A pyridine-containing ruthenium–indenylidene complex: synthesis and activity in ring-closing metathesis, J. Organomet. Chem. 691 (2006) 5444–5447, https://doi.org/10.1016/j.jorganchem.2006.08.007.
[88] T.E. Bell, G. Zhan, K. Wu, H.C. Zeng, L. Torrente-Murciano, Modification of ammonia decomposition activity of ruthenium nanoparticles by N-Doping of CNT supports, Top. Catal. 60 (2017) 1251–1259, https://doi.org/10.1007/s11244-017-0806-0.
[89] F.R. García-García, J. Álvarez-Rodríguez, I. Rodríguez-Ramos, A. Guerrero-Ruiz, F. R. García-García, J. Álvarez-Rodríguez, I. Rodríguez-Ramos, A. Guerrero-Ruiz, The use of carbon nanotubes with and without nitrogen doping as support for ruthenium catalysts in the ammonia decomposition reaction, Carbon 48 (2010) 267–276, https://doi.org/10.1016/j.carbon.2009.09.015.